MONITORING SEISMIC VELOCITY CHANGES

AT TURRIALBA

USING AMBIENT SEISMIC NOISE INTERFEROMETRY

by

Lazaro R Oliva

A thesis submitted to the Faculty of the University of Delaware in partial fulfillment of the requirements for the degree of Master of Science in Geology

Summer 2023

© 2023 Lazaro R Oliva
All Rights Reserved

MONITORING SEISMIC VELOCITY CHANGES

AT TURRIALBA

USING AMBIENT SEISMIC NOISE INTERFEROMETRY

by

Lazaro R Oliva

Approved: _____

Colton Lynner, Ph.D.
Professor in charge of thesis on behalf of the Advisory Committee

Approved: _____

John Madsen, Ph.D.
Chair of the Department of Earth Sciences

Approved: _____

Fabrice Veron, Ph.D.
Dean of the College of Earth Ocean & Environment

Approved: _____

Louis F. Rossi, Ph.D.
Vice Provost for Graduate and Professional Education and
Dean of the Graduate College

ACKNOWLEDGMENTS

I first want to thank the University of Delaware and the Geological Sciences Department for giving me the opportunity to fulfill my dreams of higher education. I thank all the people; friends, lab partners, and peers who helped me in this journey, and especially my adviser, Colton Lynner who was always there for me throughout this journey. I must also thank my fiancé Crystal O'gorman and my sweet dog Keah, which were always by my side, and my father Reinaldo Oliva who gave me the gift of studying in the United States. Finally, I want to specially dedicate this project and achievement to my mother Nilsa Hernandez, and my aunt Odalis Rodriguez, who although is no longer with us physically, made me the man I am today.

TABLE OF CONTENTS

LIST OF FIGURES

ABSTRACT

Seismic Ambient Noise Interferometry (SNI) is a prevalent tool for monitoring volcanic and associated seismic hazards. Reconstructing Empirical Green's Functions by cross-correlation (CCs) of continuous seismic noise recordings allows us to track variations in seismic wave velocity with time, providing ongoing insights into the stress state of the crust surrounding active volcanoes at depth. Most studies examine CCs of vertical components to assess velocity changes, yet velocity information extracted from the horizontal components is a great complementary investigation tool in SNI. Here we measure relative fractional seismic velocity changes (dv/v) to study the dynamics of the presently erupting Turrialba volcano as well as the crustal impacts of the 2016 Mw 5.5. Capellades earthquake. We use the MSNoise software workflow, adapted to compute the vertical (ZZ) and transverse (TT) components, to look at shear velocity changes in the crust in ten frequency bands. Our study revealed varying dv/v changes linked to the Mw 5.5 Capellades earthquake and to Turrialba's eruptive activity. Velocity changes were present in all seismic components and had strong frequency dependence. The magnitudes of dv/v changes and the overall patterns in velocity behavior observed in the vertical and transverse components varied depending on the frequency band and event type. The dv/v reduction caused by the Capellades earthquake was most prominent at higher frequency bands and was

consistent across all seismic components. The long-lived velocity reduction persisted after the event in the region until the end of our dataset. Significant decreases in dv/v followed by signal recovery were observed in association with eruptive signals. Eruptions showed more significant velocity perturbations at lower frequencies indicating deeper crustal deformation processes compared to those observed during the seismic event. Additionally, a positive change in radial anisotropy associated with eruptive signals is observed at lower frequencies. We propose that there were two instances of high magmatic fluid pulses at the bottom of the shallow magma reservoir. These pulses may have ruptured prior blockages in the conduit leading to the opening of numerous micro-cracks and increased pore-fluids. A sudden decrease in dv/v and a surge in seismic displacement during the second eruptive phase suggests that there was a higher volume of magmatic fluid influx, which ultimately led to the eruption in May 2016.

Chapter 1

INTRODUCTION

This chapter covers the primary motivation and objectives of this work (Sections 1.1 and 1.2) setting the scene for the rest of the chapters. Also, we introduced important concepts behind Ambient Seismic Noise Interferometry and its importance as a monitoring tool at volcanic settings.

1.1 Project Statement and Motivation

Volcano Turrialba is among Central America's most active and complex volcanoes. Turrialba is the southeasternmost volcano in Costa Rica's Holocene volcanic arc (Figure 1.1). It is a stratovolcano featuring explosive-type eruptions with basaltic to dacitic magma composition. This hazardous volcano is characteristic of arc volcanism at subduction zones. Its adjacency to major populated cities such as San Jose makes Turrialba a direct threat to public safety and social and economic disruption.

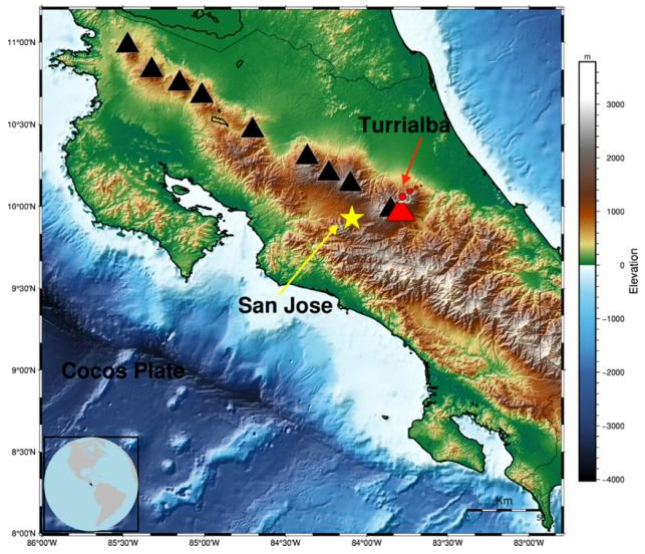

Figure 1.1: Topographic map of Costa Rica volcanism. The map shows the active volcanoes in the Guanacaste Volcanic Mountain Range (CVG) to the north, the Central Volcanic Mountain Range (CVC) in the central part of Costa Rica, volcano Turrialba (red triangle), and San Jose, the Costa Rica capital (yellow star). Notice that currently, there are no active volcanoes to the South of Costa Rica in the Cordillera of Talamanca (CTA).

Continuous monitoring of active volcanoes is critical for eruption forecasting and hazard mitigation. Scientists from different fields have used numerous surface monitor tools to improve our understanding of geological processes in volcanic settings. Approaches including thermal imaging, Global Positioning System (GPS), Interferometry Synthetic Aperture Radar (InSAR), and Tiltmeter provide valuable information about ground deformation around the summit but fail to assess the deformation of volcanic edifices at different depths (Donaldson et al., 2017).

Seismic ambient noise Interferometry (SNI) is an effective technique for examining precursory eruptive signals in volcanic settings at different crustal depths

because seismic noise is sensitive to changes in the elastic property of rocks in the subsurface (Brenguier et al., 2008; Duputel et al., 2009). Continuous seismic data allows us to measure minor temporal velocity variations in the crust surrounding volcanoes from cross-correlations of vertical and transverse seismic components. Velocity changes of Rayleigh and/or Love waves likely arise from stress perturbations in the crust leading to changes in elastic properties. My research aims to understand the crustal velocity, and therefore stress, behavior from volcanic processes and a major earthquake around Turrialba. My work will provide a detailed description of velocity changes at different depths and will inform us about variations in radial anisotropy in the subsurface. This project will address fundamental questions about stress changes in the crust beneath Turrialba and their implications for future eruptive behavior. This study will contribute to human safety by improving an effective monitoring technique to warn about volcanic reawakening to reduce the associated hazards.

1.2 Primary Objectives

Understanding the short and long-term crustal behavior of volcanic eruptive phases and seismic events is imperative to lessening their associated natural hazards. The central theme of this project is to investigate the effects of volcanic events and local earthquakes on seismic wave velocities in the crust surrounding the active Turrialba volcano to understand stress perturbations in the crust near the volcanic edifice. This work also shows the prospect of SNI as a valuable monitoring tool using both the vertical and transverse components from continuous seismic noise records.

Previously, only vertical component data has been used to examine SNI at active volcanoes. We show that the inclusion of the transverse component SNI provides invaluable additional insights. This work is guided by the following objectives and questions:

- Analyze velocity variations during eruptive stages identified using Root Mean Square Displacement (DRMS) and bulletin reports from 2015 to 2018.
- Characterize seismic velocity variations surrounding Turrialba following the 2016 Capellades Mw 5.5 earthquake (eq).
    - Is there a relationship between Turrialba's volcanic processes and the seismic event? Were there any apparent precursory signals before the main chock? Did the post-seismic recovery show a long-live velocity reduction?
- Investigate stress changes of the material at different depths beneath the volcano using Love and Ryleigh waves at different periods to identify any potential radial anisotropy changes.
- Demonstrate that information extracted from Love waves (transverse: TT component) is a great complementary investigation tool to Rayleigh waves (vertical: ZZ component).
    - Do we observe any variant behavior between the two components in the relative velocity estimation with depth?

1.3 Surface Waves

Surface waves (Love and Rayleigh waves) propagate along Earth's surface and are dispersive, given that their depth sensitivities are a function of frequency/period. Rayleigh waves result from the interaction of P and vertically polarized Sv waves with retrograde elliptical particle motions on vertical (Z) and radial (R) components. Love waves consist of horizontally polarized Sh waves and have a shear motion on the transverse component (T). The depth sensitivities of both Rayleigh and Love waves depend on velocity structure. Both become more sensitive to deeper structures with increasing periods. Using ambient seismic noise, we can extract Love and Rayleigh surface waves and use their dispersive characteristics to study the elastic properties of the subsurface at different depths beneath Turrialba.

1.4 Ambient Seismic Noise as a Monitoring Tool

Earthquakes and volcanic eruptions are two of the most striking reflection of Earth's internal processes. Collaboration of fields such as geology, geodesy, geophysics, and geochemistry provide essential insights that help us understand the mechanisms behind seismic events and volcanic eruptions. Seismic studies using teleseismic waves tend to lose high-frequency information on the recorded signal due to attenuation and scattering of seismic energy. This limits the study of shallow crustal structures, as only the high-frequency energy samples the shallowest (upper ~4km) crust. This problem is magnified in regions that are not well geographically suited to receive an even distribution of teleseismic surface waves. We can examine higher

frequency signals from ambient noise sources as an alternative to earthquake seismology to study the properties at shallow depths.

Seismic Ambient Noise Interferometry (SNI) is a prevalent and effective technique for studying volcanic eruptions (Brenguier et al., 2008). The Earth is rich in noise sources, including ocean waves, meteorological disturbances (tropical storms) (Ardhuin et al., 2011; Aster et al., 2008), glacier calving (O'Neel et al., 2007) volcanic tremors (Donaldson et al., 2017), and micro tremors in urban areas due to traffic. SNI is non-destructive and a cheaper alternative to active-source imaging for shallow targets, yet provides similar high frequency seismic data. SNI is also a great complement to ground deformation monitoring methods such as tiltmeter, GPS, and satellite imaging since it provides information about the subsurface. SNI-based studies use continuous seismic noise data for short- and long-timescale measurements. SNI uses seismic data from closely spaced stations, enhancing resolution in regional crustal studies (Shapiro et al., 2005) and continental-scale tomography (Lin et al., 2008). SNI studies rely on reconstructing Empirical Green's functions (EGF) to estimate relative velocity variations in the crust. This method has proven successful in extracting EGFs from the cross-correlation of seismic noise signals between station pairs (Shapiro & Campillo, 2004).

1.5 Cross-Correlation Functions and MSNoise

Seismic noise-based studies rely on cross-correlation functions (CCFs) between two seismic stations to calculate EGFs and changes in seismic velocities (Campillo &

Paul, 2003; Weaver et al., 2011). Perturbations impacting seismic wave velocities in the crust include geochemical changes in the material, crustal damage, temperature/pressure, fracture density, and/or subsurface structures (Donaldson et al., 2017; Olivier & Brenguier, 2016). To quantify relative velocity changes, comparing the time shift between CCFs and a defined reference CCF (Fig 1.2) for each station pair is necessary. The scattered waves that arrive after the direct surface wave are called coda waves and are used to estimate the time shift between CCFs and the reference CCF. Coda wave arrivals are dominated by scattered Rayleigh (on the ZZ) and Love (on the TT) waves and are used in SNI instead of the direct arrivals since they provide better illumination of the crust (Colombi et al., 2014) (Figure 1.2). Scattered waves can sample deep structures at lower frequencies (longer periods), but large wavelengths provide poor resolution.

Most SNI studies use CCFs from the vertical components of the seismic instruments (ZZ), which indicates Rayleigh surface wave velocity changes. Valuable information can also be extracted from changes observed on horizontal components, e.g., transverse-transverse (TT) indicating changes in surface Love wave velocities and radial-radial (RR), the horizontal component for Rayleigh waves, as shown by Flinders et al. (2020).

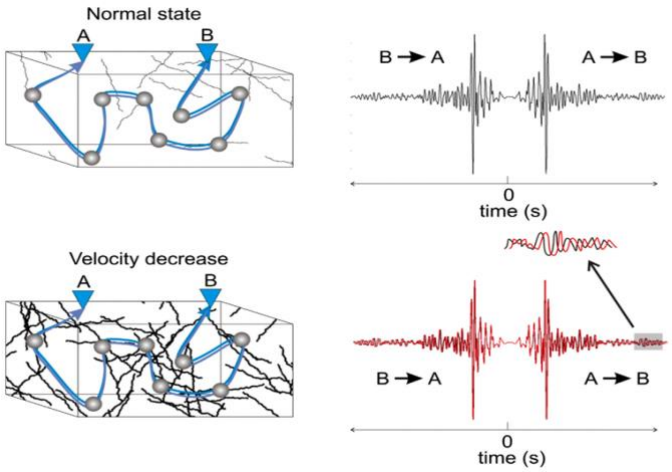

Figure 1.2: Sketch from (Brenguier et al., 2016) representing the principle of seismic velocity change detection from travel time perturbations in the coda of noise correlation functions. The top left figure represents the travel paths of late coda arrivals that originate from scattering in the complex crust. The bottom left figure represents how perturbations in the crust (cracks) affect seismic wave velocity. The top right seismogram describes the symmetric causal, and acausal Green's functions reconstructed from noise correlation. The bottom left is an example of delay time estimations from comparing the current and reference cross-correlation functions.

The use of both ZZ and TT components is valuable to assess changes in radial anisotropy in the crust. Radial anisotropy is defined by the velocity difference between vertically (Vsh) and horizontally (Vsv) polarized shear waves and provides information about the preferred orientation of structures and fractures in the crust. For example, in the shallow crust, the creation of more vertically oriented fractures causes horizontally polarized shear waves to sample slower medium (open cracks) compared to vertically polarized shear waves, which will always travel through the faster material, leading to a negative (Vsv faster) change in radial anisotropy. This mechanism is observed in the Tongariro and Ruapehu volcanoes where the intrusion

of vertical dykes produced fast Rayleigh and slow Love waves in the shallow subsurface (Godfrey et al., 2017). Multiple sets of software can be used to calculate CCFs, including Seismic Analysis Code (SAC) (Goldstein & Snoke, 2005) and Computer Programs in Seismology (CPS) (Herrmann, 2013). In this project, I am using the MSNoise software package written in Python (Lecocq et al., 2014) to obtain relative velocity variations (dv/v) in the crust from CCFs of ambient seismic noise data.

Variations in seismic wave velocities enable us to investigate the stress changes in the crust. Earthquakes and volcanic eruption processes affect the microcrack distribution in the crust, directly influencing the seismic wave velocities (Figure 1.2) (Brenguier et al., 2016; Donaldson et al., 2017). In volcanic settings, studies have attributed relative velocity changes to magma pressurization (inflation and/or deflation of the magma chamber) (Brenguier et al., 2016; Donaldson et al., 2017; Duputel et al., 2009; Mordret et al., 2010; Rivet et al., 2014) and changes in the hydrothermal system (Lénat et al., 2012; Mordret et al., 2010). After a large earthquake, a drop in seismic wave velocity has been observed in several studies caused mostly by material damage and healing processes afterward (Brenguier et al., 2008; Lesage et al., 2014; Z. Liu et al., 2014; Wu & Peng, 2011) and by pressurized pore fluids (Chaves & Schwartz, 2016). Additionally, a few studies have used frequency-dependence analysis to assess stress changes in the crust due to crustal weakening and material damage at different depths (Wegler et al., 2009; Wu et al., 2016).

In this study, we use results from ambient seismic noise interferometry to describe relative seismic velocity variations observed around Turrialba and evaluate the stress change of the crust in the region surrounding Turrialba including that impacted by the Capellades earthquake and what it may infer about future volcanic activity. Relative velocity changes are estimated following procedures from Lecocq et al. (2014). All three components of the seismic instruments are examined at different frequency bands allowing us to analyze the depth dependence of velocity changes for both Love and Rayleigh wave CCFs.

Chapter 2

GEOLOGICAL FRAMEWORK

2.1 Volcano Turrialba

Volcano Turrialba, located 65 km east of the Costa Rican capital city, San Jose, is one of Costa Rica's most active Holocene volcanoes (Figure 1.1). It is a young stratovolcano with a basaltic to andesitic composition located at the southeastern end of the arc along the central axis of the Cordillera Central. Turrialba is the tallest and most extensive stratovolcano in the region, as its edifice has a radius of around 20 km and a volume of 293 km3 (Martini et al., 2010). Turrialba shares a base and a magmatic plumbing system with its neighbor volcano Irazu which forms the largest stratovolcano complex in Central America with a volume of 372 km3 (Carr et al., 1990; Reagan et al., 2006). Turrialba has a summit depression hosting three craters and has an active magmatic-hydrothermal system (Mick et al., 2021) located in the upper 2 Km of the edifice (de Moor et al., 2016). Decompression degassing modeling outputs suggest that two magmatic sources feed Turrialba: a deep to mid-crustal reservoir at around 8~10 km depth that supplies both Turrialba and Irazu and a shallower magmatic source around 1~4 km that only supports Turrialba (de Moor et al., 2016).

The eruptive history of Turrialba dates to the 19th century during 1864-1866 (Reagan et al., 2006) when the volcano emitted ash and produced pyroclastic flows and Lahars. Small signals of reawakening started in 1996, which were progressively increasing, displaying fumarole activity at the central and southwest craters. Volcanic activity since 2007 has escalated, starting with a phreatic eruption on January 5, 2010, which opened a new vent in the Southwest Crater (Rouwet et al., 2021), followed by nearly annual phreatomagmatic explosions in 2011, 2012, and 2013 (Conde et al., 2014; de Moor et al., 2016). On October 29, 2014, the volcano started a new cycle of phreatic to phreatomagmatic eruptions with major eruptive events throughout 2015, 2016, and 2017 (Rouwet et al., 2021). The frequent phreatic volcanic activity of Turrialba is thought to be the result of the hydrothermal sealing of the system (Stix & De Moor, 2018). Turrialba's eruptive style shifted from sporadic eruptive events to more cycling eruptive phases throughout 2016 (Van Der Laat et al., 2022). After the Capellades earthquake at the end of November 2016, Turrialba became a quasi-continuously erupting open-vent system. In open-vent systems volcanoes, volatiles and gases can escape as bubbles from conduits extending to the surface (Avouris et al., 2017; Seropian et al., 2021). In this project, we identified three potential eruptive signals during our study period, defined as (a), (b), and (c) from the estimation of Root Mean Square Displacement (DRMS). Period (a) is defined as the time frame between mid-January and mid-March of 2016, period (b) as the end of April and beginning of June of 2016, and period (c) includes the time frame between September 2016 and the end of our data set on November 2017.

In addition to eruptions, Turrialba has had notable seismic activity. An important fault in the region is the strike-slip Liebres fault responsible for the Mw 5.5 earthquake (Figure 2.1) at the base of the Turrialba-Irazu complex. Seismicity at Turrialba increased as the volcanic eruptions climaxed in 2014.

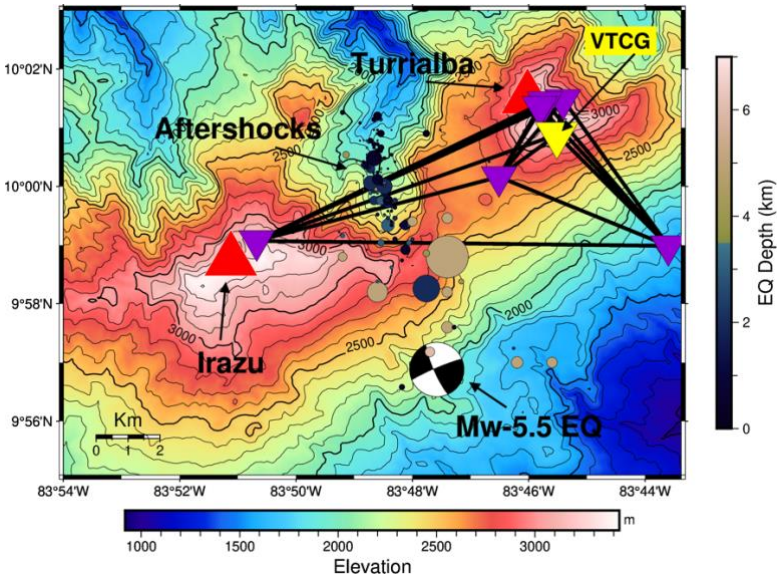

Figure 2.1: Contour map of the twin volcanoes Irazu and Turrialba (red triangles). The map shows the local network consisting of stations closest to Turrialba (purple triangles) and the corresponding noise pathways (black lines). The yellow triangle highlights the station chosen to present our DRMS measurement. The beachball or focal mechanism indicates the location and the slip mechanism for the magnitude 5.5 earthquake. The circles represent the aftershocks distribution at different depths, where bigger circles indicate higher magnitudes and smaller circles lower magnitudes. Notice the shallow nature of most of the aftershocks and their location at the base of the Irazu-Turrialba complex. Contours represent 100-meter intervals.

Fumarolic degassing and phreatic-phreatomagmatic activities produced a series of seismic swarms in the region. The largest recent seismic event at Turrialba was the magnitude 5.5 earthquake on November 30, 2016, to the North of the town of Capellades, Costa Rica (Figure 2.1) that cut across the edge of the Turrialba volcano (Linkimer et al., 2018). The hypocenter was located ~2 km deep (Linkimer et al., 2018). The moment tensor solution showed that the source was a nearly vertical strike-slip fault striking north-northwest between volcano Irazu and Turrialba. A foreshock of magnitude 2.9 was felt a day before the main event, and more than 2000 aftershocks lasted for nine days (Linkimer et al., 2018) (Figure 2.1). Aftershocks with magnitudes between 3.5 and 4.5 were registered the first days after the mainshock (Linkimer et al., 2018). These events were located around 2 km northwest of the main event epicenter at the base of the twin volcanoes, with depths ranging between 0.1 to 4.1 km (Linkimer et al., 2018) (Figure 2.1). The Capellades earthquake has been the highest magnitude event in the region since the Patillos earthquake in 1952 (Mw 6.0).

2.2 Central American Volcanic Arc

The Central American volcanic arc extends from volcano Tacaná, near the Mexican-Guatemala border, to Panama. It is often divided into nuclear Central America including the northernmost countries to the southern Isthmus (Costa Rica and Panama). The arc front trends parallel along the strike of the trench where the Cocos Plate is being subducted underneath the Caribbean plate and slips parallel to the trench north-westward at a rate of around 14+-2 mm per year relative to the Caribbean plate

(DeMets, 2001). The entire chain is landward, approximately 165 to 190 km from the trench but with variable subduction zone depths (Saginor et al., 2013). Volcanism in this region is thought to have started around the Eocene epoch within the Paleogene period, although younger (Pliocene-Quaternary) volcanoes are the dominant features (Aubouin et al., 1982). Systematic variations in geological characteristics can be observed along the entire Central American region. A thorough overview of the geology of the area can be found in (Aubouin et al., 1982; Carr et al., 1990, 2003; Protti et al., 1995).

Costa Rica lies on the western margin of the Caribbean plate between Nicaragua and Panama. The region's high tectonic and volcanic activity is driven by subduction processes along the Pacific margin of the country. Here, the Cocos plate is subducting beneath Costa Rica along the Mesoamerican Trench (MAT) at a velocity rate ranging from 69 +- 3 mm/year near northern Guatemala to 95 +- 4 mm/year around southern Costa Rica in a northeastern direction (DeMets, 2001). Northern volcanism in Costa Rica is influenced by the subduction of the Cocos plate generated at the East Pacific Rise ridge (EPR) and in central and southern Costa Rica by the plate developed at the Nazca-Cocos Spreading center (CNS).

In Costa Rica, there are three main mountain ranges: the Cordillera of Talamanca (CTA) to the south, the Guanacaste Volcanic Mountain Range (CVG) to the north, and the Central Volcanic Mountain Range (CVC) in the central part of Costa Rica where Turrialba is located. CTA was an active volcanic region until the late Miocene, e.g., (Alfaro et al., 2018), while the other two regions are currently the

active volcanic arc of Costa Rica. Over two hundred volcanic formations have been identified, with some presently active including Rincon de la Vieja, Poas, and Turrialba.

Chapter 3

BACKGROUND METHODOLOGY

This Chapter covers the background theory of the methodology used in this project. I start by giving an overview of the sources of ambient seismic noise and discussing the idea of EGFs retrieval and the pre-processing steps we should consider for more stable EGFs reconstruction. I then describe the theory behind the change in velocity measurements (dv/v) and introduce the Python software MSNoise and the different procedures taken to produce the dv/v estimations. Finally, I reconcile a series of possible mechanisms that affect seismic wave velocity in the crust due to volcanic and earthquake events from previous studies.

3.1 Ambient Seismic Noise

In this section, we cover some of the sources and principles of Ambient Seismic Noise as a monitoring tool for stress perturbation in the crust induced by geological processes such as earthquakes and volcanic activities.

3.1.1 Sources of Ambient Seismic Noise

Most seismological studies are based on seismic waves from earthquakes or explosion sources. Being dependent on earthquake distribution is particularly problematic in monitoring volcanic eruptions in regions with few earthquakes and

poor back azimuthal coverage. Examining ambient seismic noise can alleviate this shortcoming as seismic noise is ever-present and is dependent on station distribution, not event coverage. Human-generated noise, such as automobile traffic and machinery, dominates the noise spectrum for short periods between 0.1-1 seconds (Gutenberg, 1936). Other sources of short-period seismic noise include glacier calving (O'Neel et al., 2007) and wind interaction with the surface. Ocean microseisms dominate the intermediate (1-30 seconds) spectrum of ambient seismic noise. The interaction between ocean waves and the surface makes up the majority of the noise wavefield. Two spectral peaks dominate the microseism: the primary peak is around 7 seconds and originates from ocean waves interacting with bottom topography, and the secondary peak is around 14 seconds and is the product of the interaction of incoming swells with reflected waves from the coastline. At even longer periods ranging from 30 to 500 seconds, the noise signal is dominated by ocean infragravity waves, which originate from mechanisms such as the interaction between storm surges with the seafloor (Rhie & Romanowicz, 2004) or is atmospherically forced (Fukao et al., 2002).

3.1.2 Empirical Green's Function

Ambient seismic noise studies rely on extracting velocity information between different receivers. This concept is known an empirical Green's Function (EGF), where each station acts as a virtual source for the other. To estimate an EGF, we use seismic noise cross-correlations from a station pair. There have been essential

contributions outside the geological field that allow us to understand the behavior of random wavefields. For example, Aki (1957) was the first to introduce the idea of using the properties of the noise field to study Earth's structure. Also, cross-correlation to measure travel time was first applied to acoustic waves (Duvall et al., 1993). Most recently, increased seismic array densities and the ability to extract a good approximation of EGFs from noise signals have allowed us to better illuminate the crust in areas with poor earthquake coverage (Shapiro et al., 2005; Stehly et al., 2009). This breakthrough has enabled the incorporation of this method into a time-dependence investigation near volcanic settings, active regions producing earthquakes, and reservoir monitoring.

The EGF theory assumes uncorrelated and homogeneous distribution of noise wavefield (Equipartitioned noise) (Campillo & Paul, 2003; Snieder, 2004). In real Earth, many factors impact the recovery of the EGF, including non-stationary sources, heterogeneity, anisotropy, instrument drift, and attenuation. Well-documented studies describing the effect of such factors include e.g., (Fichtner, 2014; Tsai, 2009). Despite potential shortcomings, many studies have demonstrated that cross-correlation positively retrieves EGF approximations from the noise wavefield (Snieder, 2004; Tsai, 2009).

Multiple processing and stacking schemes can be adopted to improve the overall quality of the EGF estimation. A key component is to stack together a long duration of ambient noise data to make the noise sources more homogeneously distributed e.g., (Lin et al., 2008; Yang et al., 2007). Time-domain and spectral normalization can also

be performed on the waveforms to reach measurement stability by improving the signal-to-noise ratios (SNR). Time-domain normalization is a particularly important processing step to improve the SNR since it suppresses contaminating signals, such as surface waves from seismic events or random noise. Different schemes for time-domain normalization include the running absolute mean normalization where a running average normalizes the signal, 1-bit normalization where the raw trace amplitude becomes (+-1) depending on the sign of the original signal, and finally the Root Mean Square (RMS) clipped waveform that we use in this work. Frequency domain whitening is also essential to maximize the bandwidth of observations in the ambient noise field. Frequency whitening will balance all the frequencies' energies and eliminate confounding precursory signals. In this work, we use spectral whitening, which diminishes the outsized influence of the ocean-wave microseism in the cross-correlation functions relative to the smaller high-frequency energy (Bensen et al., 2007).

3.2 Measuring Seismic Velocity Changes

Seismic velocity variations are estimated following the approach of (Poupinet et al., 1984). The method is applied to cross-correlation functions between a pair of receivers to track relative velocity changes (dv/v) from travel time perturbations. The main idea is to compare cross-correlation functions stacked over short moving windows with a reference cross-correlation function produced using a long and stable

period of the noise record. The relative time shift between the current and reference cross-correlation functions assesses the relative velocity estimations by the relation:

$$\frac{dt}{t} = -\frac{dv}{v} \qquad (3.1)$$

assuming a homogeneous seismic velocity variation in space. This analysis focuses on the coda arrivals of the noise correlation function between a pair of receivers. Unlike direct arrivals that propagate directly from the source, coda waves originate from scattering in the crust (Figure 1.2). Scattered waves travel longer paths in the crust sampling a higher volume of the medium. They are therefore more suitable for shallow targeted studies since they are highly sensitive to small stress perturbations providing a better illumination of the crust.

3.3 MSNoise and Data Processing

To go from raw waveforms to dv/v estimation, I am using the free, open-source software MSNoise written in the Python language (Lecocq et al., 2014). This software has been used in multiple studies in different settings and has a straightforward workflow, which is described in the MSNoise documentation (Lecocq et al., 2014) and summarized below. The processing approach to estimate seismic velocity variations in the crust using MSNoise can be divided into three main stages: (1) Data preparation and preprocessing, (2) CCFs for individual station pairs at different dates and temporal stacking of the CCFs and (3) relative travel time delay estimation (dt/t) (Figure 3.1).

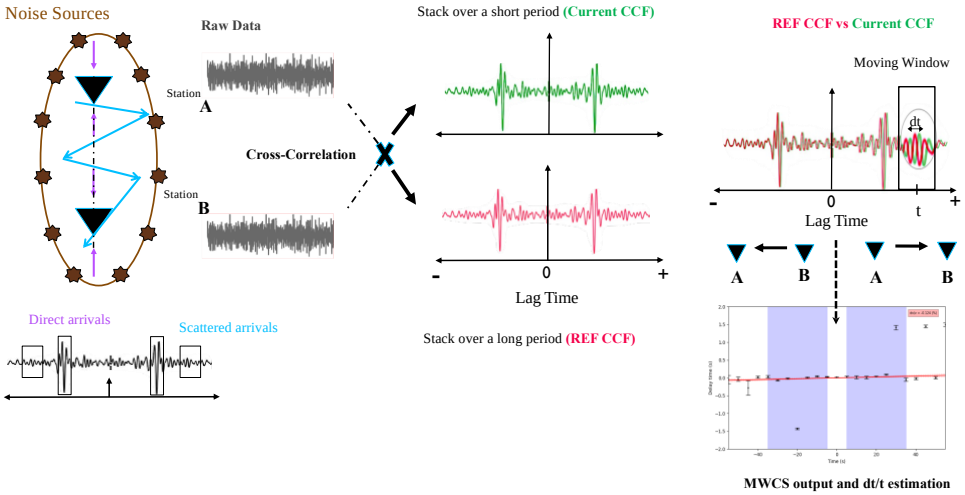

Figure 3.1: Illustration of the process for estimating travel-time delays (dt/t) for a pair of seismic receivers A and B from delay time (dt) measurements between two time series at each moving window segment within a lag time range (t). This cartoon follows the workflow of the MSNoise software used in this project.

To initialize a project, we first create a database in MySQL that will interact with the software throughout the analysis. The day-long raw seismograms are organized and properly renamed before being scanned into the data archive. MSNoise will then locate and read the files using Obspy (Beyreuther et al., 2010; Tobias Megies et al., 2011) and insert them in the data availability table. MSNoise will then define all possible cross-correlation jobs for each station pair to be processed. For an n number of stations, there will be:

$$\frac{n(n-1)}{2} \qquad (3.2)$$

pairs to compute.

Once all the cross-correlation jobs are defined, the waveforms are preprocessed and analyzed. Each one-day-long trace is demeaned and tapered, and the trace is padded with zeros in case of any data gaps. The signal is then downsampled to 20 Hz and bandpass filtered with the configured high and low-frequency filters. Before computing a cross-correlation function, time-domain and spectral normalization are performed to improve the cross-correlation estimation and remove unwanted signals such as those produced by earthquakes. The user may use 1-bit normalization or clip the signal to an integer value of the trace's Root Mean Square (RMS). In this study, we decided to clip the signal to three times RMS. Spectral whitening is applied between a very wide frequency range (0.01Hz to 8Hz, well beyond the periods used in the dv/v estimation) to broaden the bandwidth and flatten the amplitude spectrum of ambient noise.

After performing all the preprocessing steps, waveforms corresponding to interstation pairs are cross-correlated on the different components for each of the different filters and for each defined 30-minute window. It is necessary to compute all three components of ground motion to extract information from Rayleigh and Love waves, that is, cross-correlation functions from the Vertical (V), Radial (R), and Transverse (T) directions of ground motion. MSNoise will rotate the East (E) and North (N) components based on the azimuth (az) of both stations to calculate the R and T orientations. The cross-correlation operation is made in the frequency domain. The cross-correlation computations are then stacked using a linear stacked method to produce a daily CCF.

In MSNoise, we define a period for the reference cross-correlation in the configuration file. The reference stack should be taken over a long and stable period. We stack daily cross-correlation functions to suppress the random-noise (not seismic noise) content of the signal and obtain more reasonable velocity estimations. Although stacking multiple cross-correlations will improve the signal-to-noise ratio, using larger moving-window stacks will decrease the temporal resolution of any signal (G. Liu et al., 2009). We are interested in short-term velocity variations; thus, the high temporal resolution of the signal is imperative in our study. We compute 1, 2, 5, and 10-day moving-window stacks to compare with the reference stack to work around this trade-off. The stack results show that using a 10-window stack provides the best resolution for our interpretation of the current dataset and parameters.

To estimate delay times, MSNoise uses the Moving Window Cross Spectral analysis technique (MWCS) introduced by (Ratdomopurbo & Poupinet, 1995) and further improved by (Clarke et al., 2011). The MWCS method works in the frequency domain to assess the similarity of the current and reference CCFs. The two time-series are compared, mean adjusted and cosine tapered in each window before transforming the time-series to a frequency domain using Fourier Transformation. The similarity of the two signals is then assessed in the frequency domain using the cross-coherence between energy densities. The delay time between the two time-series is the slope of a Weighted Linear Regression (WLR) within a specific frequency band. The result will be a table of delay time measurements at each window within a lag time range. A

detailed description of this technique and the accuracy of MWCS in velocity variation estimations can be found at (Clarke et al., 2011).

We use the delay time results from the MWCS step to estimate the relative velocity variations (dv/v). The dv/v of the whole network is estimated from the average of the delay times using all the noise pathways. The average of the entire network provides a better representation of crustal features since individual station pair measurements are more variable (Figure 3.2).

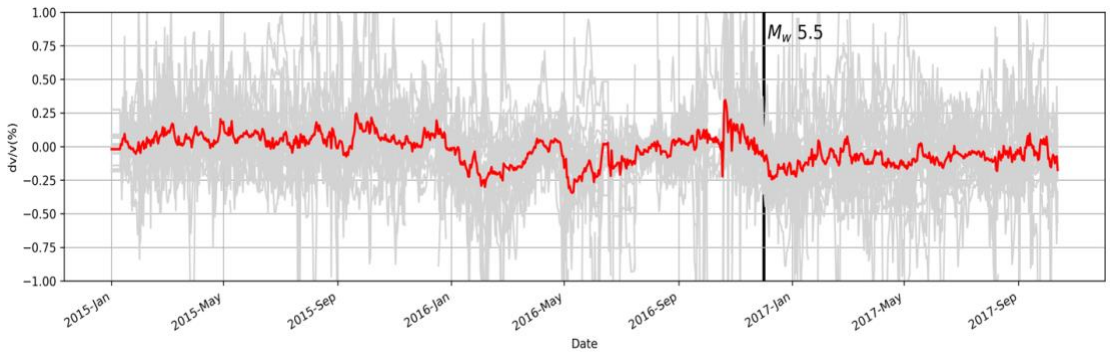

Figure 3.2: Average relative velocity variation (dv/v) of the whole seismic local seismic network (red time series) and each individual inter-station path dv/v (light gray time series). The black vertical line marks the timing of the Mw 5.5 Capellades earthquake. The plot highlights the variability of individual station pair measurements and the necessity of estimating the average dv/v to be able to interpret subsurface crustal features in the region.

For time shift computations, we only use delay time measurements that fall within a configured minimum (5s) and maximum (35s) lag time (Table. 1). We selected this lag time window to avoid the ballistic wave arrivals (near time 0) and use the cross-

correlation function's late coda arrivals (Figure 1.2 and 3.1). The interstation distance plot (Fig. 6) helps us decide which parameters to use in the relative travel time variations estimations.

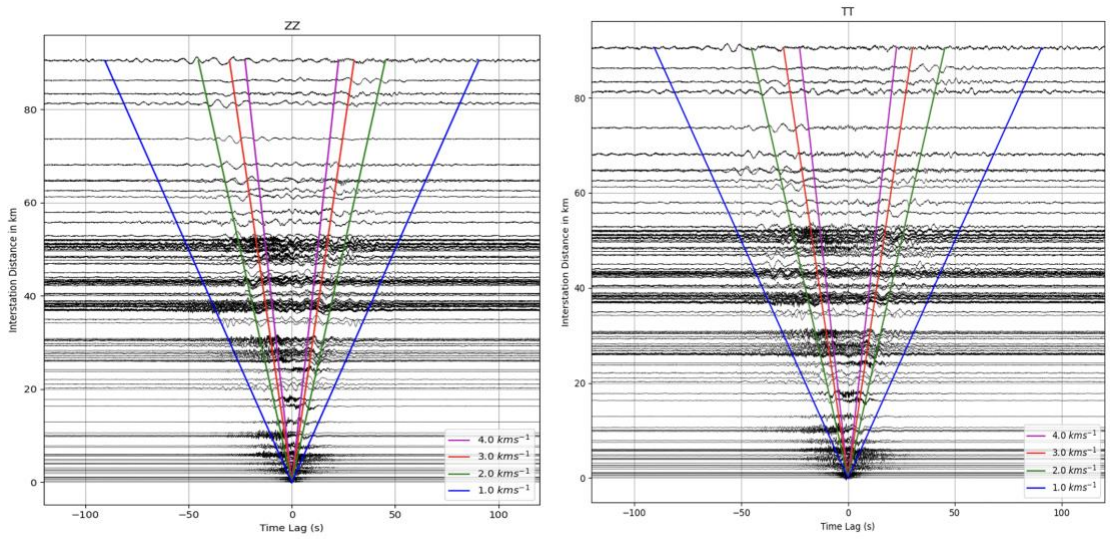

Figure 3.3: Stacked reference CCF for each Turrialba station pairs ordered by interstation distance of the ZZ (right plot) and TT (left plot) component plotted as a function of lag time for the frequency range 0.6 to 0.8 Hz. The blue, green, yellow, and red lines indicate the moveout of different shear velocities. Notice that the ballistic waves are visible in the velocity range of 2 to 4 km/s.

Using Figure 3.3, we decided to use a minimum lag time of 5 s for our analysis since the ballistic waves are visible in a velocity range of 2 to 4 km/s. We only consider points satisfying a configured maximum error and minimum coherence threshold.

We estimate travel time variations as the slope of delay times against lag times using a weighted linear regression (WLR). The WLR is calculated by forcing the

regression through the origin. Figures 3.4 and 3.5 show examples of this process for the vertical and transverse components of the station pairs RIMA-VTCG and OCM-VTRT before the main seismic event on November 30, 2016. The blue bands represent the lag time interval used to fit the regression line. In Figure 3.4, a negative slope (right plot) indicates a velocity increase, and a positive slope (left plot) a velocity decrease in that station pair for that day. The illustration in Figure 3.1 resumes the process of estimating travel-time delay (dt/t) for a pair of receivers.

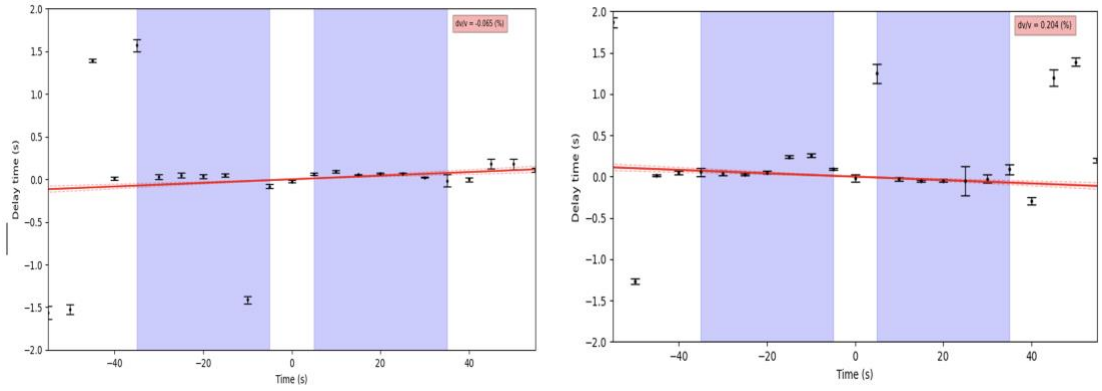

Figure 3.4: Moving-window cross-spectral analysis example for the ZZ (left) and TT (right) component, with a slope (red line) and its uncertainty (dashed red lines) fitted to delay times measurements (black points) and their errors (error bars) for station pair RIMA-VTCG on November 22, 2016. A filter of the interval 0.6-0.8 Hz was applied to the waveforms, and they were stacked over 10-days moving windows. Shaded bands define the lag time periods that are used in the calculation of the regression line at positive and negative lag times.

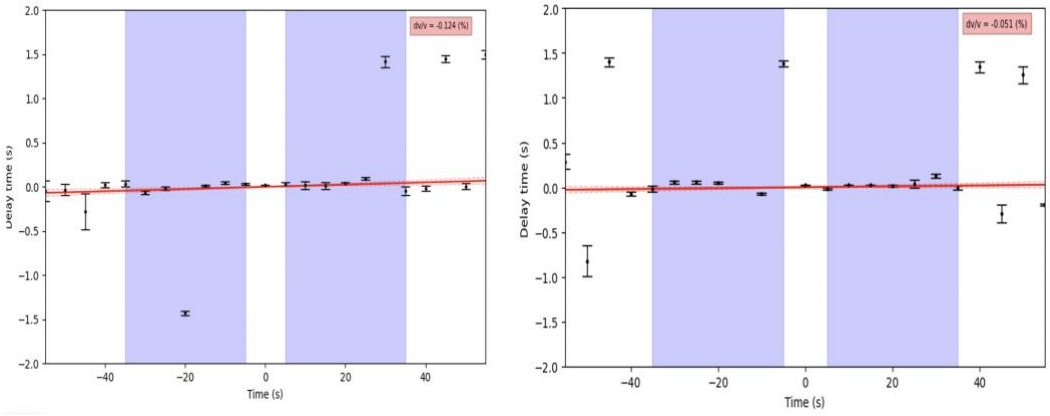

Figure 3.5: Moving-window cross-spectral analysis example for the ZZ (left) and TT (right) component, with a slope (red line) and its uncertainty (dashed red lines) fitted to delay times measurements (black points) and their errors (error bars) for station pair OCM-VTRT on November 22, 2016. A filter of the interval 0.6-0.8 Hz was applied to the waveforms, and they were stacked over 10-days moving windows. Shaded bands define the lag time periods that are used in the calculation of the regression line at positive and negative lag times.

3.4 Mechanism Affecting Seismic Wave Velocity in The Crust

Valuable insights about the stress distribution in the crust can be extracted from earthquake-related co-seismic and post-seismic velocity observations. Many SNI studies have shown a rapid decrease in seismic wave velocity during an earthquake event followed by a slow post-seismic recovery process (Brenguier et al., 2008; Q.-Y. Wang et al., 2017). Material damage from shallow dynamic shaking followed by post-seismic stress relaxation is the primary mechanism behind earthquake-related velocity changes, as Wu et al. (2016) showed in their San Andreas fault zone study. The energy in the seismic wave induced by an earthquake propagating through the crust causes a dynamic stress perturbation in the surrounding material resulting in the opening of

micro cracks and fractures, which subsequently leads to a velocity reduction. Q. Wang et al. (2019) used frequency-dependent analysis on the Tohoku-Oki earthquake to show a decrease in co-seismic and post-seismic seismic wave velocity at short periods associated with strong ground shaking in the region.

In volcanic settings, the interaction of rising volcanic material with the surrounding rocks impacts the stress field of the crust. Seismic velocity changes are influenced by the variation of microcracks distribution associated with the compression and dilation of the volcanic system. As the system compresses, pressure increases, closing pre-existing microcracks and pore spaces thereby increasing seismic wave velocities. Precursory velocity increases associated with the dilation and compression of volcanic systems have also been observed in different studies (Donaldson et al., 2017; Duputel et al., 2009; Mordret et al., 2010; Rivet et al., 2014). An opposite seismic velocity response to the same volcanic mechanism was observed by Brenguier et al. (2008), which shows a seismic velocity decrease before eruptions of volcanoes at Piton de la Fournaise interpreted as the effect of the dilation process resulting from magma movement. In this work, we investigate what may be responsible for the varying seismic velocities around Turrialba during eruptive episodes. The spatial stress distribution from the volcanic system also needs to be considered in the interpretation. Using different frequency bands and seismic components is crucial in our analysis as it provides a means to distinguish between deeper and shallower variations.

Chapter 4

METHODS

In this chapter, we explain the procedures and parameters used in this project to estimate relative changes in seismic wave velocity (dv/v) using raw seismic records from noise sources and the estimation of Root Mean Square ground motion displacement (DRMS) from probabilistic power spectral density (PPSD) calculations of a single seismic station. We included the DRMS to better identify potential eruptive signals during the study period.

4.1 Data Source

We used continuous seismic data recorded at 14 broadband seismic stations of the Observatory Volcanological and Seismological of Costa Rica (OV) operated by the National University of Costa Rica located within a radius of 50 kilometers (km) from Turrialba (Figure 4.1). This network started sharing data with the IRIS DMC in November 2014 and ended in January of 2018. To quantify changes in relative seismic velocities using scattered Rayleigh and Love surface waves, all three components of the seismic instruments were downloaded: vertical (Z), North (N), and East (E). We analyzed the dataset from January 2015 to January 2018. This time includes the Capellades M_w 5.5 earthquake as well as several eruptive events. This time range

allowed us to have a stable reference period before the earthquake and main eruptive signals. For DRMS calculations, we used the vertical components of the 7 broadband seismic stations located on top of the volcanic edifice (Figure 2.1).

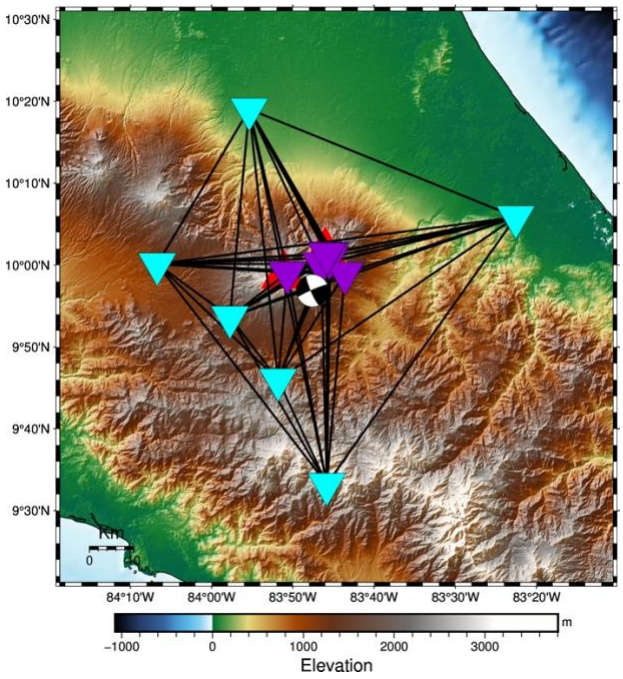

Figure 4.1: Topographic map of the study area, showing the broadband seismometers of the regional network (colored triangles) and the local network (purple triangles). The black lines represent the corresponding noise pathways between the seismic stations. The map also shows the Irazu volcano (left red triangle), Turrialba volcano (right red triangle), and the M_w 5.5 Capellades earthquake (beach ball).

4.2 Relative Velocity Change Estimation Procedure

The analysis procedures follow those of Lecocq et al. (2014) using the MSNoise software package workflow described above and in Figure 3.1. First, we downloaded

broadband three-component (Z, N, and E) seismic noise data for all stations and renamed them to the appropriate data structure. The data is scanned into an SQL database to create the noise cross-correlation jobs. All the stations are populated with their respective coordinates and elevation in the database. We did not remove the instrument response since the instruments did not change during the study period (Lecocq et al., 2014). Each seismic trace is demeaned, tapered, and organized into 1-day-long segments during waveform preprocessing. The 100 Hz data is then downsampled to 20 Hz using the ObsPy Lanczos resampler. The 1-day-long trace is cut into 30-minute segments, low and high-passed between 0.01-8.0 Hz, and a 1-bit normalization and spectral whitening in the time and frequency domain were applied respectively.

CCFs for all the components are then computed for the 91 interstation pairs for each daily stack. To retrieve the radial-radial (RR) and transverse-transverse (TT) components, the N and E seismic station components are first rotated using the station's coordinates. The results are then stacked over 10-day moving windows to obtain the current daily CCFs. Comparing daily CCFs to the reference CCF produces substantial variations due to the high random-noise content of the daily CCFs. We define the reference CCF by stacking the cross-correlations over a period from February 1, 2015, to November 1, 2016. This selected range for our reference CCF is discussed in the section below. Delay times between reference and daily CCFs were estimated using a Moving Window Cross Spectral analysis (MWCS) approach (Clarke et al., 2011). To bound the depth of the velocity variations, ten frequency bands were

used: (0.2-0.4); (0.4-0.6); (0.6-0.8); (0.8-1.0); (1.0-1.2); (1.2-1.4); (1.4-1.6); (1.6-1.8); (1.8-2.0) Hz and a wider frequency range (1.2-2) Hz.

We tested the influence of different reference (REF) cross-correlation functions in our results by running our analysis using different REF time periods. We tested REF periods including: 1) the six months before the earthquake event to look specifically at variations in velocity due to the seismic event, 2) the first 10th months of 2015 to look at eruptive signals during 2016, 3) a similar REF to that ultimately chosen but excluding January 2015 from our analysis, and 4) finally using the entire time frame following the approach taken by previous studies. We ultimately determined that a REF from February 1, 2015, to November 1, 2016, yielded the most reliable and consistent results while highlighting the earthquake and eruptive features. We are confident in our results because all the features that we interpret below are present regardless of the REF choice.

4.3 Ground Motion Displacement Calculation Procedures

We calculated root mean square displacement (DRMS) on top of Turrialba as a complementary interpretation tool to our dv/v estimations. We use DRMS as a proxy for volcanic eruptive phases. The data processing to estimate DRMS was performed following the previous methodologies and using the publicly available SeismoRMS software package (Lecocq et al., 2020). We modified the codes to estimate daily average DRMS displacement.

We used continuous vertical seismic recordings from the 7 broadband stations that are located on Turrialba (Figure 2.1). We obtained similar DRMS patterns across the seven stations and show station VTCG in the figures (Figure 2.1). We first downloaded the waveform data from the IRIS DMC for each day and computed the probabilistic power spectral density (PPSD) using Welch's method (Welch, 1967) for an 1800s-time window with a 50% overlap. Then, we converted the PPSD measurements to an average daily PPSD and processed it to extract the DRMS from the time-domain displacement. Finally, we estimated the average daily DRMS in the same frequency domains used in the dv/v calculations.

Chapter 5

RESULTS

We processed three years of seismic data using 14 stations with 91 inter-station paths over our study region. We defined this network as “regional” due to its broad coverage of the Turrialba region (Figure 4.1). We subdivide our dataset into a "local" network consisting of the seven closest stations to the volcano, providing coverage of 21 inter-station paths that cut through the volcanic edifice and the region directly impacted by the Capellades earthquake (Figure 2.1). Despite the differences in coverage, our findings indicate that both networks display similar dv/v patterns across various frequency ranges. However, the magnitude of dv/v change in the regional network is considerably lower since many paths do not sample the volcanic edifice or near the Liebres fault (Figure 5.1).

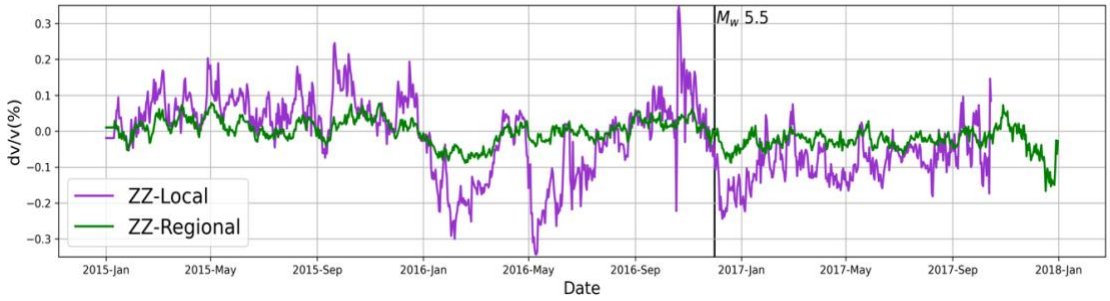

Figure 5.1: Average relative velocity variation (dv/v) of the regional seismic network (green time series) and the local seismic network (purple time series). The dv/v for both seismic networks were estimated in the vertical component (ZZ) in the 0.6-0.8 Hz frequency band. The black vertical line marks the timing of the Mw 5.5 Capellades earthquake. Notice the difference in the magnitude of dv/v change between both networks. The local network highlights better the volcanic crustal features we discuss in this project.

The earthquake dv/v signal remains prominent regardless of the network used. We present our findings based on the local network because its paths are more responsive to local crustal features. Consequently, the results from this seismic network provide better insight into the local crustal properties associated with volcanic eruptions.

5.1 Earthquake Event

Our study revealed varying dv/v changes linked to the MW 5.5 Capellades earthquake and Turrialba's eruptive activity (Figure 5.2). To identify periods of eruptive signals, we cross-referenced bulletin reports and published scientific papers with changes in DRMS.

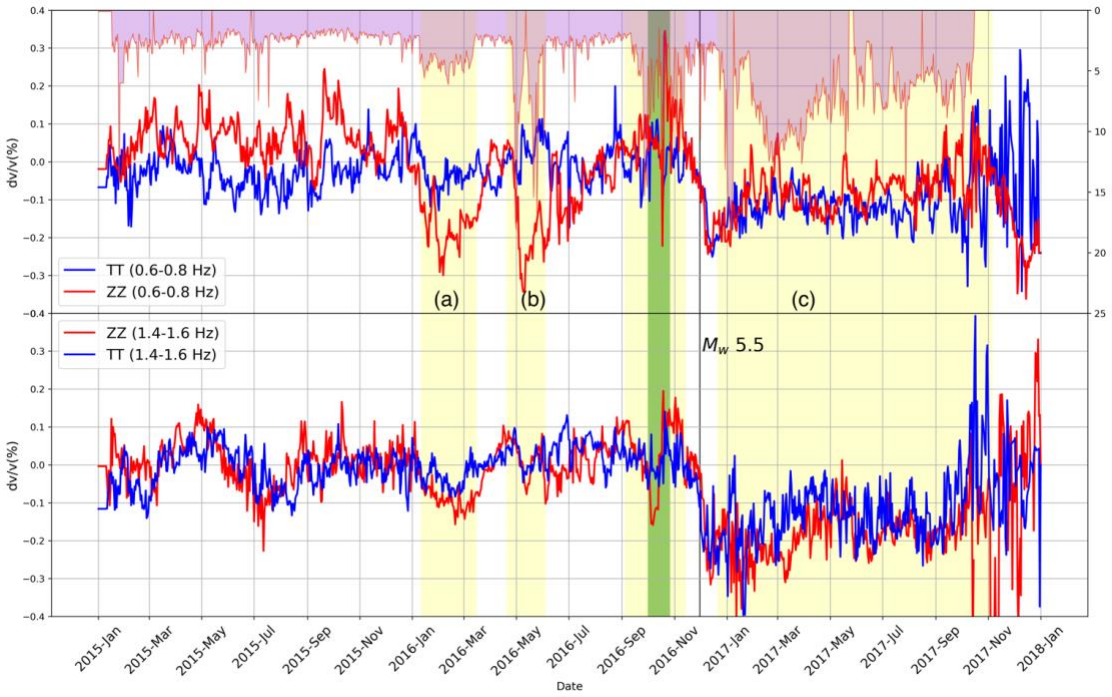

Figure 5.2: Average relative velocity variations (dv/v) for Turrialba's local seismic network associated with the Mw 5.5 Capellades earthquake (black line) and three eruptive signals (yellow bars) identified as (a), (b), and (c). Dv/v records are for the ZZ (red) and TT (blue) components in the low-frequency band 0.6-0.8 Hz (top panel) and high-frequency band 1.4-1.6 Hz (low panel). Ground motion displacement DRMS (shaded purple area) was extracted from the Power Spectral Density (PSDs) of the signal. The green bar during the eruptive signal (c) highlights a period of less noise-pathway density coverage. Notice the varying dv/v behavior of the signal for both components depending on the type of event (seismic and eruptive signal), and frequency bands (low and high).

The dv/v variations were observed in both ZZ and TT components across various frequency bands (Figure 5.3). The magnitude of dv/v change for both components varied depending on the event type and the frequency band. Notably, the differences in

trend between ZZ and TT were more pronounced for eruptive events than for earthquake signals and are frequency dependent (Figures 5.2 and 5.3). During eruptive events, there is a distinguishable divergent dv/v behavior between ZZ and TT at lower frequency ranges while the two components trend more similarly at higher frequency bands (Figure 5.2). Additionally, although the magnitude of dv/v change varied depending on the frequency ranges within the low and high bands, the overall patterns remained consistent (Figure 5.3). To simplify our analyses, we refer to frequency bands below 1 Hz as low-frequency bands and those above 1 Hz as high-frequency bands. We utilized the 0.6-0.8 Hz frequency band as the lower-frequency range and 1.4-1.6 Hz as the higher-frequency range to present and discuss our findings (Figure 5.2). A decrease in dv/v associated with the Mw 5.5 Capellades earthquake is evident in both the ZZ and TT components across all frequency bands (Figure 5.3). The drop in dv/v varies in magnitude with frequency. A more pronounced decrease of ~0.4 % is observed at frequency ranges above 1 Hz, and a smaller drop of ~0.2 % is visible at lower frequency ranges, such as 0.6-0.8 Hz (Figures 5.2 and 5.4).

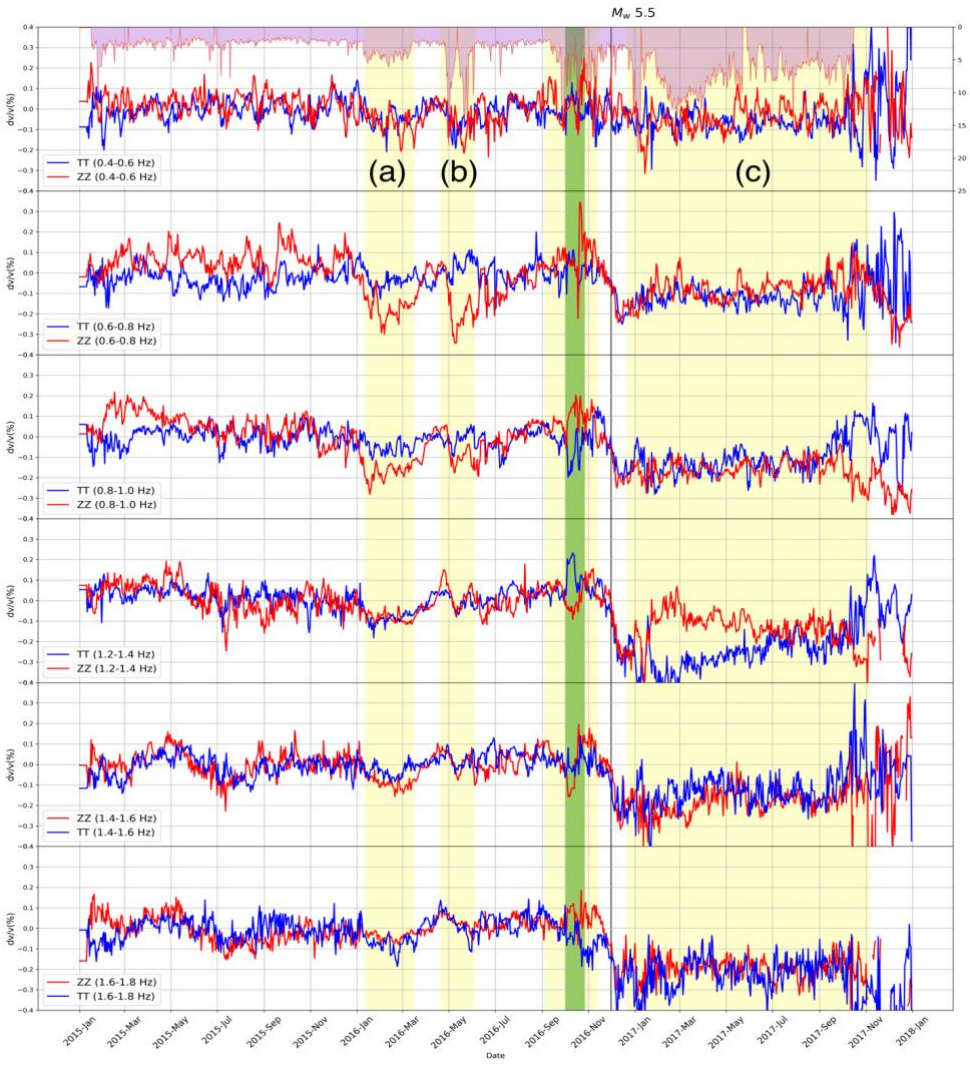

Figure 5.3: Average relative velocity variations (dv/v) for Turrialba's local seismic network associated with the Mw 5.5 Capellades earthquake (black line) and three eruptive signals (yellow bars) identified as (a), (b), and (c). Dv/v records are for the ZZ (red) and TT (blue) components in six frequency bands: three-low frequency ranges (top three plots) and three-high frequency ranges (bottom three plots). Ground motion displacement DRMS (shaded purple area) was extracted from the Power Spectral Density (PSDs) of the signal. The green bar during the eruptive signal (c) highlights a period of less noise-pathway density coverage. The figure highlights the frequency-dependency nature of the dv/v signal related to the seismic event and eruptive signal. Notice that the overall dv/v pattern for both seismic components is consistent within the low-frequency bands (less than 1 Hz —top 3 plots) and the high-frequency band (greater than 1 Hz—bottom 3 plots).

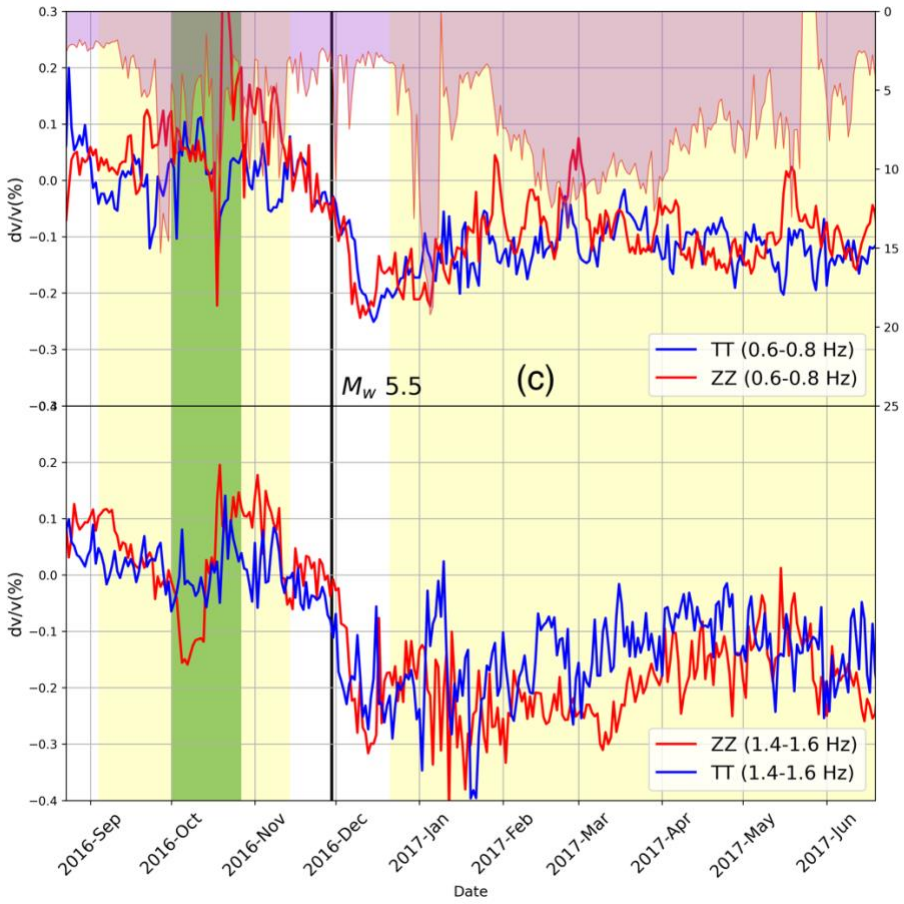

Figure 5.4: Zoomed in version of Fig. 11 to highlight features related to the earthquake event and eruptive signal (c). The plot shows the average relative velocity variations (dv/v) for Turrialba's local seismic network associated with the Mw 5.5 Capellades earthquake (black line) and eruptive signals (c) (yellow bar). Dv/v records are for the ZZ (red) and TT (blue) components in the low-frequency band 0.6-0.8 Hz (top panel) and high-frequency band 1.4-1.6 Hz (low panel). Ground motion displacement DRMS (shaded purple area) was extracted from the Power Spectral Density (PSDs) of the signal. The green bar during the eruptive signal (c) highlights a period of less noise-pathway density coverage. Notice the velocity reduction in both seismic components and the more pronounced drop at higher frequency bands (bottom panel). For both frequency ranges, the velocity begins dropping a few days before the main event coincides with the beginning of the eruptive signal (c) and elevated DRMS. A long-lived velocity reduction in the region is observed in 2017 after the earthquake.

This velocity reduction is consistent in both ZZ and TT seismic components and shows similar trends regardless of the frequency range or network. This pattern is also observed in individual interstation paths, as seen in the dv/v map in Figures 5.5 and 5.6, which shows that the entire volcanic edifice area experienced a negative change in dv/v after the earthquake.

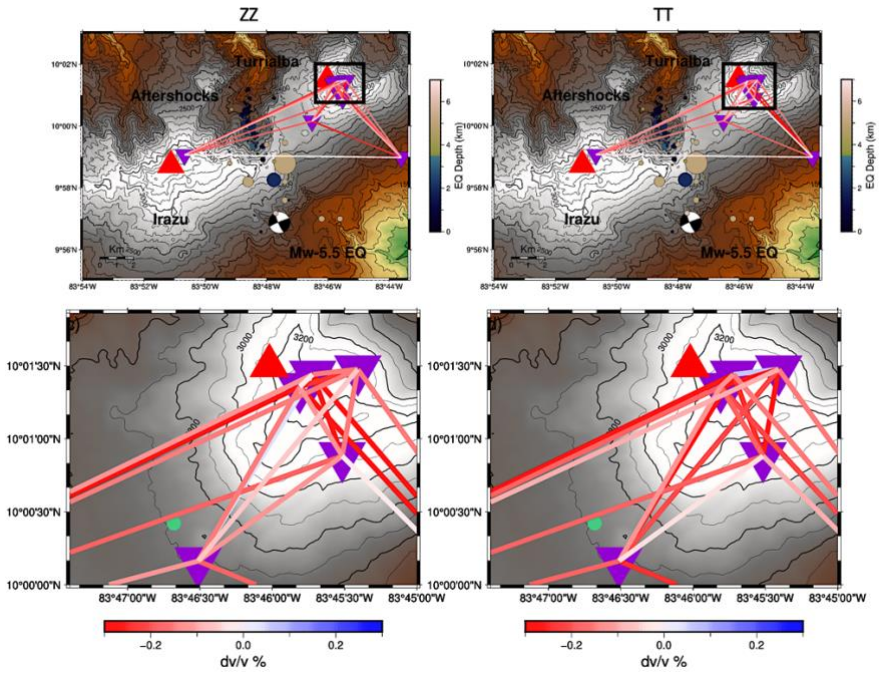

Figure 5.5: Interstation paths of the local seismic network colored to show the average relative velocity variations (dv/v) distribution in the region associated with the Mw 5.5 Capellades earthquake. Dv/v records are for ZZ (left maps) and TT (right maps) components in the 0.6-0.8 Hz frequency band. For each path, velocity variations were estimated from the difference between 10 days' dv/v average before and after the EQ (a 10-day trailing time was left after the earthquake corresponding to our 10-day moving stack). The maps show a velocity reduction in each seismic path suggesting overall crustal damage at the volcano summit associated with the seismic event. Also, notice that the velocity reduction is consistent in both ZZ and TT components.

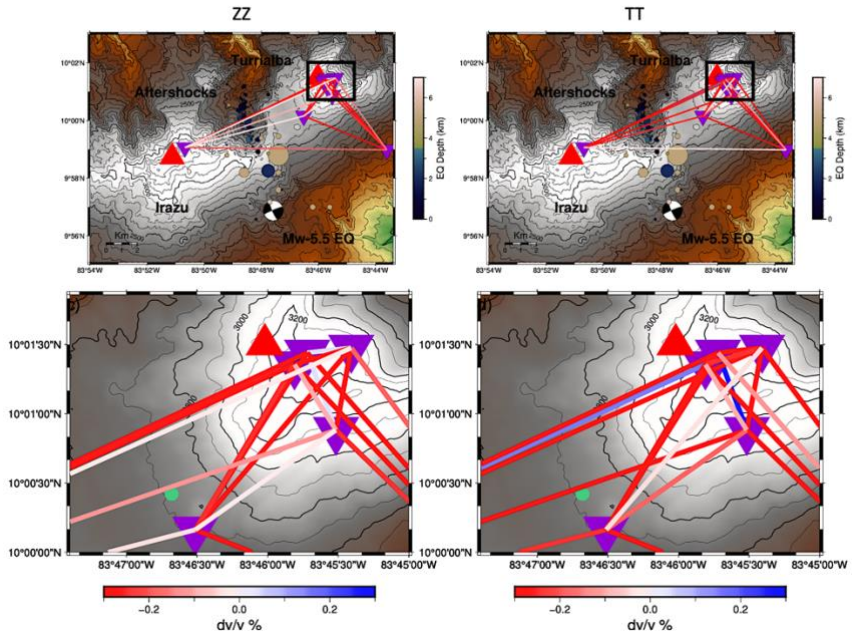

Figure 5.6: Interstation paths of the local seismic network colored to show the average relative velocity variations (dv/v) distribution in the region associated with the Mw 5.5 Capellades earthquake. Dv/v records are for ZZ (left maps) and TT (right maps) components in the 1.4-1.6 Hz frequency band. For each path, velocity variations were estimated from the difference between 10 days' dv/v average before and after the EQ (a 10-day trailing time was left after the earthquake corresponding to our 10-day moving stack). The maps show a velocity reduction in each seismic path suggesting overall crustal damage at the volcano summit associated with the seismic event. The magnitude of the velocity reduction at this high frequency is greater than those at lower frequency ranges. This is consistent with our average dv/v observations at frequency bands greater than 1 Hz. The velocity reduction pattern in both ZZ and TT components is consistent regardless of the frequency ranges.

Additionally, the velocity reduction associated with the earthquake seems to initiate ~15 days before the main seismic event. This precursory drop coincides with the conclusion of a period of high DRMS in November 2016. The velocity reduction after the event persisted for approximately three weeks, followed by a recovery

process lasting 15-20 days. The velocity recovery during this period was faster at higher frequencies and was followed by a rapid dv/v drop coinciding with an impulsive DRMS signal during the first week of January 2017 (Figure 5.2). Subsequently, the dv/v remained stable and did not return to its initial value by the beginning of 2018 in either the high or low frequencies. The dv/v patterns following the seismic event are similar in both ZZ and TT components for all frequency bands, except for the 1.2-1.4 Hz frequency band. In this frequency band, after the abrupt dv/v drop (fourth panel of Figure 5.3), the velocity increase in the ZZ component was faster and remains elevated compared to that found in the TT component. Elevated DRMS suggests this is an unstable time period and may be impacted by quasi-continuous nature of the eruptive activity after the seismic event (Van Der Laat et al., 2022).

5.2 Eruptive Signals

We also found varying changes in dv/v associated with periods of increased DRMS and eruptive signals in both the ZZ and TT components across different frequency ranges (Figure 5.3). Unlike what was seen with the earthquake, the amplitude of dv/v variations were more prominent at lower frequency bands than in higher frequencies. In early 2016, a period of high DRMS lasted from mid-January to mid-March. This period was characterized by isolated small ash emissions, explosions, and an increase in volcanic tremors (Van Der Laat et al., 2022). During this period, there was a decrease in dv/v across all frequency ranges in both the ZZ and TT components. The velocity reduction was more pronounced at lower frequency bands,

indicating deeper depth deformation (Figures 5.3 and 5.7). The onset of velocity drop occurred in early January and persisted for approximately a month until dv/v started to increase again in early February. The reduction in velocity at low frequencies was around 0.4% in the ZZ component which doubled the smaller decrease of approximately 0.2% observed in the TT component (Figure 5.7). However, both components showed similar trends at frequency ranges above 1 Hz. By the first week of April, the dv/v signal in both components had returned to background levels near 0% (Figure 5.7).

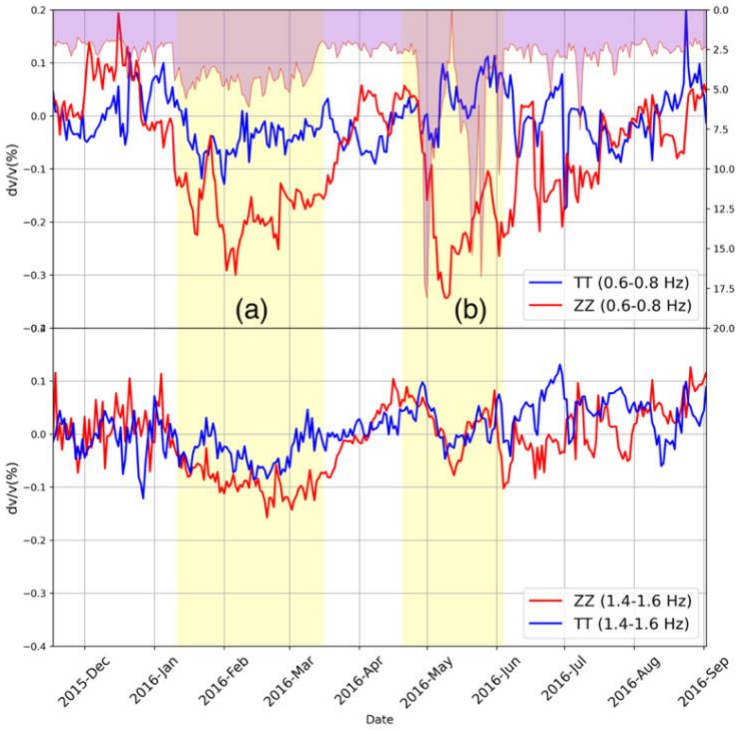

Figure 5.7: Zoomed in version of Fig. 11 to highlight features related to the eruptive signals (a) and (b). The plot shows the average relative velocity variations (dv/v) for Turrialba's local seismic network associated with the eruptive signals (a) and (b) (yellow bar). Dv/v records are for the ZZ (red) and TT (blue) components in the low-frequency band 0.6-0.8 Hz (top panel) and high-frequency band 1.4-1.6 Hz (low panel). Ground motion displacement DRMS (shaded purple area) was extracted from the Power Spectral Density (PSDs) of the signal. The figure shows how the overall dv/v pattern and magnitude of change are frequency dependent. There is more response to crustal deformation at lower frequencies (deeper depth) than at higher frequency ranges (shallow depth). This observation is the opposite of what was found for the earthquake event (Fig. 11, and 13). Also, at lower frequencies, dv/v observations for ZZ and TT show a positive radial anisotropy behavior while both time series trend similarly at higher frequency ranges.

During the first 20 days of April, there were no significant changes in dv/v observed and DRMS remained low indicating a period of relative quietness. At the end of April, a sharp increase in DRMS was detected coinciding with a rapid and

short-lived dv/v drop of ~0.4% at frequencies lower than 1 Hz. The dv/v reduction was found in the ZZ component and lasted for about 10 days until it began to increase again, returning to background levels (Figure 5.7). In contrast, the TT component showed a slight increase in dv/v ~0.15 %. This anisotropic behavior was observed in almost all individual paths of the local network shown in the dv/v map of Figure (5.8). Here, the TT component shows a positive change in dv/v, while the ZZ component shows the opposite. This pattern is frequency dependent and is not observed at frequency bands greater than 1 Hz, where results from both components closely correlate in dv/v magnitude of change and trend (Fig 14 a and b). During the dv/v recovery process beginning in early May, a pattern seemed to repeat across frequency bands: an increase in dv/v lasting for ~20 days followed by a rapid decrease correlating with another high DRMS pulse. A slower dv/v increase was then observed until reaching background levels at the end of July.

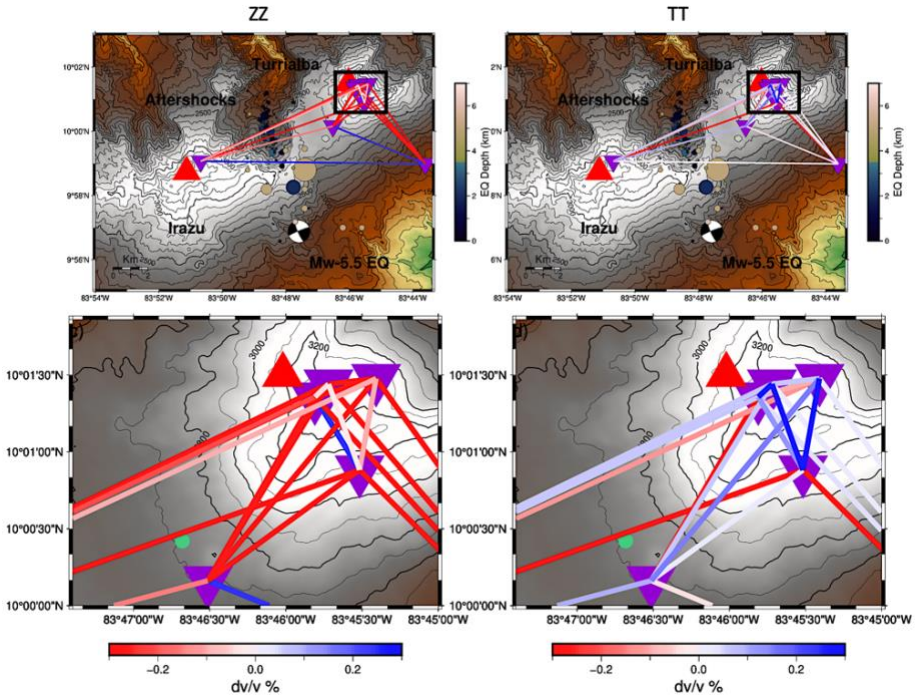

Figure 5.8: Interstation paths of the local seismic network colored to show the average relative velocity variations (dv/v) distribution in the region associated with the eruptive signal (b). Dv/v records are for ZZ (left maps) and TT (right maps) components in the 0.6-0.8 Hz frequency band. For each path, velocity variations were estimated from the difference between 10 days' dv/v average before and after the EQ (a 10-day trailing time was left after the first DRMS pulse corresponding to our 10-day moving stack). The maps show a positive radial anisotropy behavior at this frequency range. A velocity reduction in most seismic paths on top of the volcano summit in the ZZ component is observed, while a positive velocity pattern is observed in the TT component.

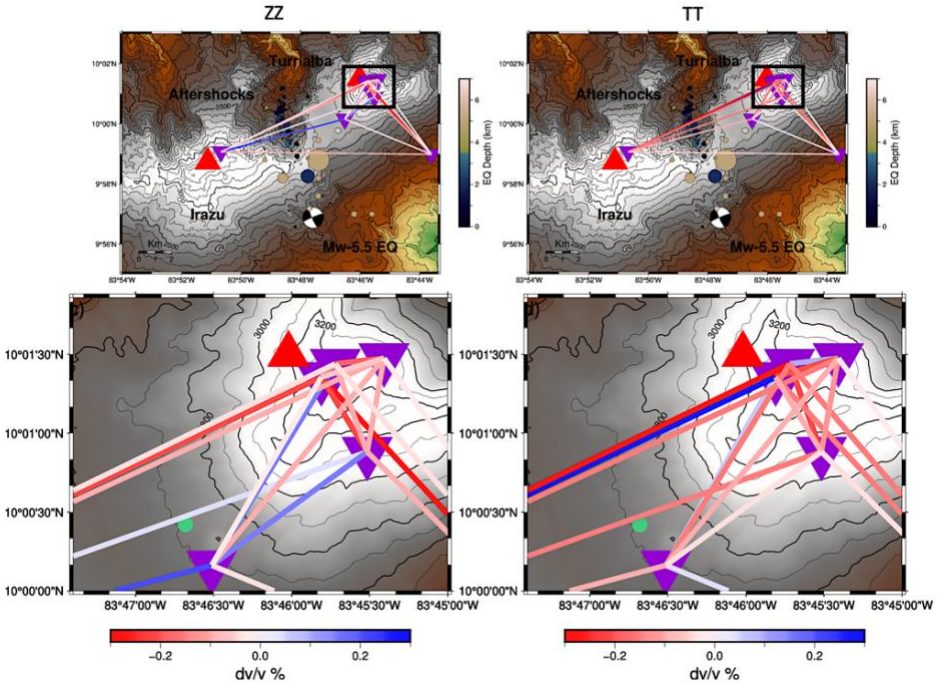

Figure 5.9: Interstation paths of the local seismic network colored to show the average relative velocity variations (dv/v) distribution in the region associated with the eruptive signal (b). Dv/v records are for ZZ (left maps) and TT (right maps) components in the 1.4-1.6 Hz frequency band. For each path, velocity variations were estimated from the difference between 10 days' dv/v average before and after the EQ (a 10-day trailing time was left after the first DRMS pulse corresponding to our 10-day moving stack). The maps show a similar dv/v trend on seismic paths on top of the volcano summit at high frequencies. The dv/v estimation for both ZZ and TT components correlate closely at this frequency range which is the opposite of what was found at low-frequency ranges (Figure 5.8). The observations in Figures 5.8 and 5.9, show a clear dv/v frequency-dependent pattern associated with the stress perturbation induced by volcanic activity in the region.

From August to September 2016, there was another period of relative quietness with no significant changes in dv/v. However, at the beginning of October, the daily average DRMS increased and remained unstable until mid-November. Our dv/v measurements of the local network showed varying patterns across frequency bands

and components during this period. Several measurements, unfortunately, did not pass quality control checks resulting in lesser path density available to estimate the average dv/v of the region during this event (Figure 5.10).

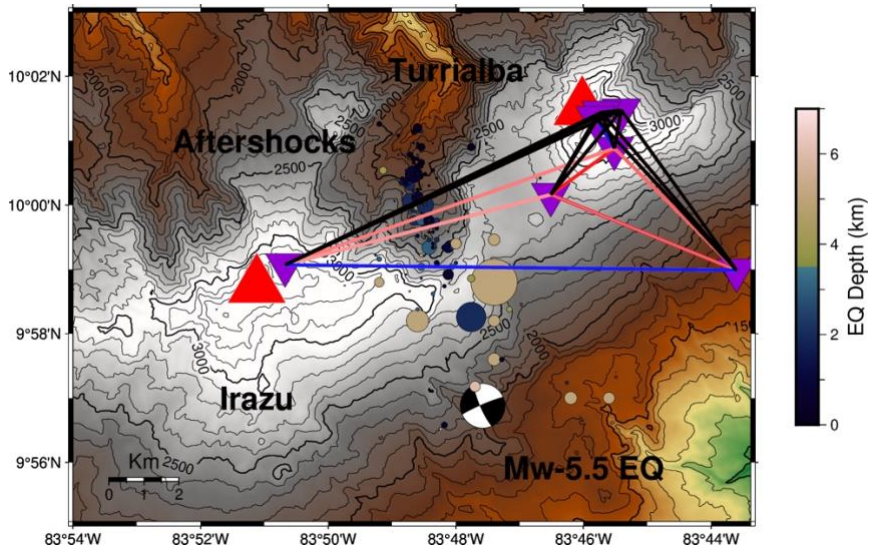

Figure 5.10: Interstation paths of the local seismic network showing the noise path (black lines) that did not pass our quality control checks during the period highlighted with a green bar during eruptive signal (c) (Fig. 11, 12, and 13). Note that during this eruptive signal period (c), there is less path density for dv/v estimation on top of the volcano summit. This pattern is consistent across all frequency ranges.

Therefore, we use the entire regional network to help us identify dv/v patterns during this unstable period. We observed a short-lived decrease in dv/v of approximately 0.2% across all frequencies during the first week of October, coinciding with an increase in DRMS. This lasted for around 15 days, followed by a velocity increase until the first week of November. Overall, both seismic components exhibited

this pattern with a small variation in magnitude change. There is more variation in the local network, where at some frequencies e.g., 0.8-1.0 and 1.2-1.4 Hz, ZZ and TT behave differently with uncharacteristic dv/v jumps (Figure 5.3). However, this is likely attributed to due to poor data coverage and greater measurements error during this time.

Following the Capellades earthquake, there is a recovery period of approximately one month where dv/v gradually returns to its background level, and DRMS remains stable. In the first few days of January 2017, however, there is a sudden dv/v drop of ~0.3 % in both seismic components that coincides with high DRMS extending through January 20, 2017. The velocity reduction is visible across frequency bands and is more prominent at frequencies greater than 1 Hz (Figures 5.2 and 5.3). After this drop, a dv/v increment in the ZZ component peaks with a high DRMS around February 25 in the 1.2-1.4 frequency band. During the same period, TT shows a mirroring polarity behavior, and the signals ultimately reach similar levels by the end of 2017. Throughout the rest of 2017, DRMS remains elevated, and dv/v remains low, never returning to background levels. There are no significant changes in dv/v observed in any component across frequency bands.

Patterns in dv/v measurement errors were consistent throughout our results in both components ZZ and TT. Large errors are found during periods when few seismic inter-station paths passed our quality control step, e.g., minimum coherence on time delay measurements. Also, larger errors are produced in periods with elevated DRMS due to the background noise of the ambient noise field. In addition, dv/v measurement

errors in the TT component show no significant difference from those observed in the ZZ component (Figure 5.11). The average error for the whole data set in the ZZ and TT components is 0.110 and 0.104 respectively. This is important to assess the quality and accuracy of our dv/v estimations in the TT component.

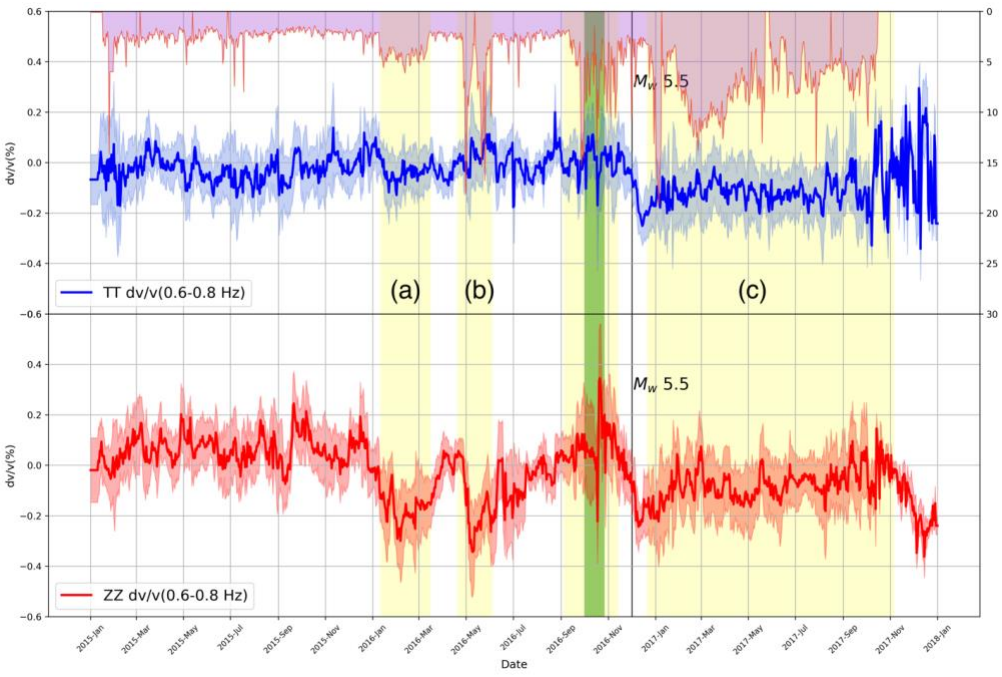

Figure 5.11: Relative seismic velocity variations (dv/v) in the TT (top blue plot) and ZZ (bottom red plot) component using a 10-day moving window stack in the 0.6-0.8 Hz frequency band. The black vertical line marks the date of the Mw 5.5 earthquake, and the three eruptive signals (yellow bars) are identified as (a), (b), and (c). Light blue and red shading areas indicate the error in the measurement at each data point, estimated using weights and the square misfit to the modeled slope. The errors for each day were estimated as the average errors for all the corresponding seismic interstation paths. The pattern in dv/v measurement errors is consistent throughout our results in both ZZ and TT components. During periods of high DRMS, the errors are slightly greater.

Chapter 6

DISCUSSION

We used continuous ambient seismic noise records and inter-station noise cross-correlation to calculate long-term dv/v measurements in the Turrialba region (Figures 2.1 and 4.1). This method enabled us to analyze and interpret changes in seismic velocities over time in relation to volcanic eruptions and earthquakes. Our approach included the TT component in addition to the commonly used ZZ component, which added robustness to our findings.

6.1 Crustal Response to The Earthquake

In this study, we found a sharp, temporal decrease in seismic velocity in Turrialba associated with the large (Mw 5.5.) regional Capellades earthquake (Figures 5.2, 5.3, and 5.4). The drop in velocity occurred in different frequency ranges, indicating that the earthquake affected materials at varying crustal depths (Figure 5.3). Following the earthquake, there was a long-lived seismic velocity reduction in Turrialba. By the end of our study period, velocities never returned to their pre-earthquake dv/v levels (Figure 5.2). Mechanisms such as crustal damage and healing processes have been attributed to the observed changes in velocity after large earthquakes (Brenguier et al., 2008; Lesage et al., 2014; Z. Liu et al., 2014; Rubinstein

& Beroza, 2005; Wu et al., 2016). These mechanisms are related to dynamic stress perturbations from waves propagating after an earthquake and are based on the theory of cracks opening and closing or reduced packing within weak layers, which has been demonstrated in laboratory experiments (Wu et al., 2016).

The Capellades earthquake induced the largest seismic velocity drop at higher frequency bands, suggesting more deformation occurred at shallower depths (Figures 5.2 and 5.4). This aligns with the seismic event's shallow rupture of ~2 km and subsequent aftershocks, where most of them were localized in the upper 2 km of the crust at the base of the Irazu-Turrialba complex (Figure 2.1). Although the velocity reduction was present in the regional network, it was more significant in the local network. Additionally, significant velocity reductions were measured for paths that cross the volcanic edifice but don't sample the area near the Libres fault (Figure 2.1 and 5.1). This observation suggests that in addition to the velocity disturbances caused by the damage from the strike-slip fault, there is also crustal damage in the shallower layers of the volcanic edifice. While the connection between the earthquake and the magma feeding system remains unclear, it is possible that the weaker structure of the magmatic plumbing system may have contributed to greater deformation and local dv/v reduction. Additionally, several aftershocks were located at the base of the Irazu-Turrialba complex. While dynamic stress perturbations weaken with the square of distance, the biggest dv/v drops are actually observed on paths around the volcanic structure (Local network). The similar pattern of velocity reduction in ZZ and TT across the various frequency ranges (Figure 5.3) indicates that the crust underwent

deformation that did not have a preferential orientation in either the vertical or horizontal planes. The microcracks created by the rupture of the earthquake were likely randomly distributed in the damaged area.

6.2 Relationship Between Volcanic Processes and Earthquake

The slight decrease in dv/v that was observed several days before the primary seismic events could be associated with volcanic processes from the October-November 2016 eruptive event (Figures 5.2 and 5.4). This precursory signal might have been a consequence of the static stress disturbance induced by fluid movement within the Turrialba system. Fluid flow within a volcano's plumbing system can influence permeability, leading to microcracks in the structure due to the pressurization of the system, thereby decreasing the seismic velocity. While the fluid dynamics beneath Turrialba is not well understood, there are reports of long-period (LP) and harmonic tremor events during this period (Van Der Laat et al., 2022) that likely indicate the presence of deeper moving fluids. It is uncertain whether there is a direct correlation between magmatic-hydrothermal fluids in the rupture mechanism of the earthquake or if it was just the result of regional stress impacting the Liebres fault (Linkimer et al., 2018). Previous studies based on volcanic-tectonics and geodesy data have postulated the potential connection between the Capellades earthquake and magmatic intrusion and hydrothermal fluids since the Liebres fault is thought to be located between the deeper and shallower magmatic reservoirs feeding the eruption (Van Der Laat et al., 2022). More physical modeling in the area is needed to evaluate

the interplay between magmatic intrusion, the surrounding environment, and the rupture mechanism.

There is stronger evidence regarding the impact of the Capellades earthquake on the eruptive behavior of Turrialba. Perturbations in volcanic settings induced by seismic waves from earthquakes can modify volcanoes' eruptive cycles and degassing processes. Numerous studies have demonstrated how large earthquakes may act as degassing triggering mechanisms at active volcanoes (Avouris et al., 2017; Seropian et al., 2021). Our study found that by the end of 2017, only half of the seismic velocity reduction had been recovered and that both seismic components exhibited a leveled dv/v shape (Figure 5.2). This suggests either a very slow post-seismic recovery process beyond the scope of our data or that permanent damage is pervasive in the upper crust. During 2017, stations located at the summit of the volcano displayed unstable DRMS measurements, which may indicate continuous and quasi-eruptive cycles from consistent fluid movement within the system. This pattern was not seen before the earthquake during 2015-2016 when DRMS measurements showed alternating eruptive signals and periods of quietness (Figure 5.2). Previous volcanological studies in the region have demonstrated changes in the volcanic system to an open-vent eruption style since January 2017 (Alvarado et al., 2021; Van Der Laat et al., 2022).

6.3 Crustal Response to The Eruptive Signals

We identified three potential eruptive phases (a), (b), and (c) in Turrialba based on DRMS estimations (Figure 5.2). The crustal velocity response to stress perturbations during these phases varied across different frequency bands. In contrast to the earthquake, the most significant dv/v variations related to eruptive signals were detected at lower frequency bands, indicating deeper crustal perturbations compared to those observed for the Capellades event (Figures 5.2 and 5.3). While the depth constraints for our dv/v results are not well resolved, previous studies have suggested that a shallow magma reservoir exists at depths between ~2-4 Km. This implies that our dv/v measurements related to eruptive signals may come from depths where the shallow magma chamber is located. Furthermore, the varying velocity patterns between ZZ and TT suggest a favored orientation of crustal structures in response to perturbations generated by volcanic processes.

The first eruptive signal (a) was detected from mid-January to the first week of February 2016 (Figures 5.2 and 5.7). During this time, a significant decrease in dv/v was observed at lower frequency measurements, coinciding with elevated DRMS. The decrease in velocity was not associated with any surface eruptions, as only occasional explosions and ash emissions were observed throughout this period. Rather, this period was marked by a high level of seismic activity, including volcanic tremors, low-frequency (LP), and very-low-frequency (VLP) events (Van Der Laat et al., 2022). The velocity reduction could be the result of cracks opening due to volcanic fluid movement within the system either from the deeper (~8km) reservoir or

migration from the neighboring Irazu volcano toward Turrialba. Although ZZ and TT both showed a decrease in dv/v, the reduction was far more pronounced in the vertical component, indicating a greater crack density in the horizontal plane supporting lateral movements of fluids through horizontal pathways.

The period leading up to the eruptive episode (b) on April 29, 2016, was marked by a continuous increase in dv/v over the course of approximately two months followed by a stable signal for 15 days and low DRMS (Figures 5.2 and 5.7). The increase in velocity over this time is likely attributed to the compression of the volcanic system due to the gradual inflation of the shallow magma chamber. The increased pressure causes the closure of pre-existing microcracks, leading to an increase in seismic velocity. Ground observations made by GPS stations at the volcano summit have identified similar inflation processes at Turrialba (Battaglia et al., 2019). An alternative explanation for the increase in dv/v leading up to the second eruptive signal is that the volcanic system remained under compression, but there was a depletion of magmatic fluids stored in the crust beneath the shallow magma chamber. As a result, open fractures would have closed, and the rock would have become more compact. This is consistent with the greater increase in dv/v observed at lower frequencies. At high frequencies, there is still a small increase in dv/v, which may be due to the inflation of the system and possibly influenced by a shallow hydrothermal system. However, at greater depths where the increase in dv/v is more significant, other processes beyond just inflation would likely be impacting the seismic velocity. This is discussed in the next section.

In late April 2016, a second eruptive signal (b) was identified with two pulses of DRMS (Figures 5.2 and 5.7). The first pulse was accompanied by a rapid short-term seismic velocity reduction in the ZZ component, which suggests rapid magma movement within the shallow reservoir. The deeper nature of the velocity reduction suggests deformation from magmatic fluids entering the shallow magma reservoir. As magma migrates from the deeper reservoir below ~8km, it may damage the surrounding rock at the base of the shallow magma chamber. This would reopen cracks and lead to a decrease in seismic velocity. During event b), there were records of LP, VLP events, and harmonic tremors, which all reinforce the involvement of magmatic fluids in the system (Van Der Laat et al., 2022). While other potential mechanisms such as the collapse or rapid decompression of the plumbing system could also lead to a decrease in seismic velocity (Donaldson et al., 2017), there is little eruptive evidence to support this. GPS observations do not indicate any dilation of the system during this time (Battaglia et al., 2019). The second pulse of DRMS is associated with intense volcanic explosions and increased gas and ash emissions, which coincides with a gradual increase in dv/v (Figures 5.2 and 5.7). This long-term velocity recovery may be due to the closing of cracks during the healing process, as gas is released from the system and there is weaker magma migration from the deep reservoir.

During this second eruptive signal (b), the seismic velocity in the ZZ component experienced a sudden decrease, while a more stable dv/v signal was observed in the TT component. This differs from the dv/v pattern caused by the Capellades

earthquake, which showed consistent velocity variations in both components. In eruptive signals, there is a unique dv/v pattern in both components that is frequency-dependent and exhibits changing anisotropic behavior at deeper depths (lower frequencies). Weeks before the eruptive signal (b) on April 27, 2016, the velocities in both components were stable. After the increase in DRMS, a velocity decrease of ~0.4% was observed in the ZZ component, while the TT component showed an increase in dv/v of ~0.15% (Figure 5.7). This change in radial anisotropy suggests that there is a preferred orientation of open pores and microcracks in the horizontal plane, which may have been caused by the stress induced by the high pressure of magmatic fluids. The presence of horizontal layering of old lava flows may also play a role in the preferred orientation of structures surrounding the shallow magma chamber. Other studies have suggested horizontal layering to interpret positive radial anisotropy (Vsh > Vsv) in volcanic settings (Mordret et al., 2015). Studies of long-period (LP) seismic events in Turrialba suggest a highly fractured area with fluid saturation and the presence of sub-horizontal shallowing dipping cracks (Zecevic et al., 2016), which may be consistent with our observations. Our results at higher frequencies indicate that stress perturbations from volcanic processes at shallower depths did not lead to a prefer orientation of changes in crustal structures or fractures (Figures 5.2, 5.3 and 5.7). This change in the variation of radial anisotropy with depth suggests variable crustal deformation is induced by volcanic processes. This may be enhanced by horizontal structures at deeper depths. This may be an important detail in constraining

the directional and flow dynamics of the magmatic-hydrothermal system underneath the Irazu-Turrialba complex.

Our DRMS estimations further identified an eruptive signal (c) from October 2016 until the end of our dataset (Figures 5.2 and 5.4). This is a period that includes the Capellades earthquake and represents a potential relationship to Turrialba's eruptive processes. We have discussed the potential relationship between the earthquake and Turrialba's eruptive processes in the previous section. Before the earthquake, a high DRMS period showed small changes in dv/v across frequencies. However, some frequencies showed inconsistent dv/v changes (Green block in Figures 5.2, 5.3, and 5.4) this may be due to fewer inter-station paths used for the dv/v estimation due to several being rejected by our quality control steps in the time window (Figure 5.10). Further work is required to make a conclusive interpretation of the volcanic processes during this period.

6.4 Preferred Model: Two High Volcanic Fluid Pressure Pulses

The Turrialba volcano has two magma reservoirs at different depths, a shallow chamber between 2-4km depth and one deeper than ~8km, and a shallow magmatic-hydrothermal system (Stix & De Moor, 2018). The supply of new magma, volatiles, and heat from a deeper region into the shallow magma chamber can disturb the system by inducing an increase in pressure (Roman & Cashman, 2018). When the transport of deep magmatic fluids through the conduits leading to the shallow magma chamber stops, the system will potentially recover as the surrounding rocks will recover to their

original shear velocities. Surface deformation and seismicity observation from the effect of an over-pressurized system and magma migration could provide important insights about imminent volcanic eruptions (Cayol et al., 2000; Taisne et al., 2011). Additionally, the seismic wave velocity-stress perturbation dependency in the crust allows us to study the temporal evolution of deep mechanical properties in volcanic settings (Ratdomopurbo & Poupinet, 1995). We propose that a similar stress perturbation mechanism caused the velocity variations observed at Turrialba during the main eruptive signals (a) and (b) (Figures 5.2 and 5.7). This model involves a potential conduit blockage being opened by two instances of high volcanic fluid pressure pulses at the base of the shallow magma chamber. This ultimately led to the volcanic eruption in May 2016 when a critical volume of eruptive magmatic fluids was reached. Our proposed model is explained in detail below and illustrated in Figure 6.1.

Stages (**a**) and **(b**) display a recurring pattern of a sharp velocity reduction followed by a gradual recovery. We propose that during the first stage (**a**) (**Fig. 14**), the pressure at the bottom of the shallow magma chamber increased from input of fresh magmatic fluids from the deeper magma reservoir. This high fluid pressure potentially fractured a conduit blockage that formed when a previous magmatic influx stage ceased. This would produce an impulsive DRMS signal, LP events, and a rapid decrease in dv/v consistent with what we observe.

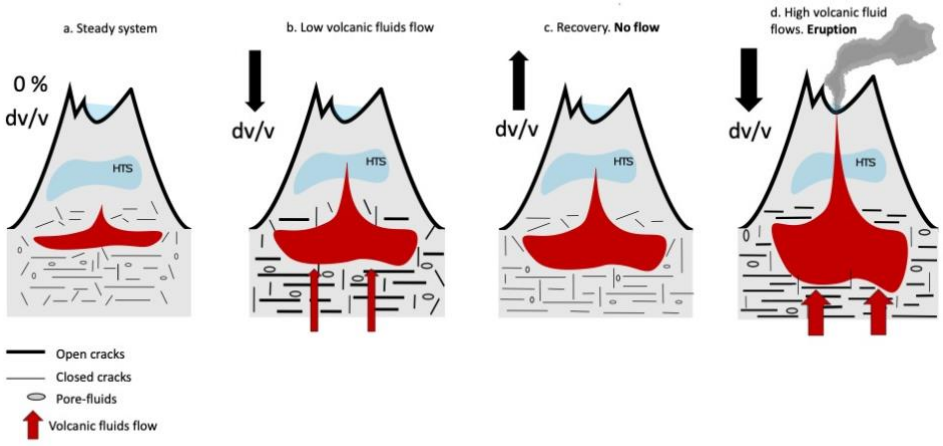

Figure 6.1: Illustration showing our preferred model for the relative velocity variation (dv/v) behavior in ZZ and TT associated with the eruptive signals (a) and (b). The system began in a steady state with no dv/v variation ~ 0 % (Figure 5.2) before the first eruptive signal (a). This was followed by a small volume of volcanic fluid inputs disrupting the system and opening a few subhorizontal structures in the crust causing an overall velocity reduction. A period of signal recovery with potentially no volcanic fluid flow at the base of the shallow magma chamber is observed during c. Lastly, the high magmatic fluids input from the down reservoir during the eruptive signal (b) caused a greater stress disturbance in the system, opening new subhorizontal structures in the crust as observed by the positive radial anisotropy during this instance. During this eruptive phase (b), the higher volume of volcanic fluid migrating from the down reservoir was sufficient to trigger the eruption in May 2016.

The replenishment of material into the shallow magma chamber will result in overall dilation creating cracks in the surrounding rock and leading to a decrease in seismic velocity (Figure 5.7). The intrusion of magma during this phase, however, was not accompanied by eruptive activity. We believe this was due to insufficient amounts of volcanic fluid inputs to trigger an eruption. The subsequent increase in dv/v implies the surrounding rock was allowed to undergo healing and return to its original shear

velocity state. We propose a similar process occurred during the second eruptive stage (b). The impulsive ground displacement signal and the sharper velocity drop saw with (b) suggest that a larger pulse of new magma breached the bottom of the reservoir (Figure 5.7). The influx of magma led to more significant deformation of the surrounding rock as was sufficiently voluminous to trigger an eruption at the surface. This time, the introduction of fresh material into the shallow magma chamber was sufficient to trigger the eruption in May 2016. The second impulsive DRMS signal during this eruptive signal (b) could have been influenced by the interaction between the magmatic fluid and the shallow hydrothermal system, resulting in continuous phreatic eruptions. However, dv/v results at high frequencies do not show significant changes in velocity at shallower depths (Figures 5.2, 5.3, and 5.7). This may be attributed to a water-saturated region where it is more challenging to alter the strain of the rock (Figures 5.2 and 5.7).

The seismic velocity reduction during the eruptive signal (b) is observed on the ZZ component, while dv/v exhibits a minor increase in the TT component (Figures 5.7, and 5.8). The varying behavior of the ZZ and TT components indicates the predominance of new horizontal structures in the crust. The mechanism driving this positive change in radial anisotropy at lower frequencies in Turrialba is uncertain. One possible explanation is the impact of high volcanic fluid pressure from the deeper reservoir reducing the vertical effective stress of the horizontal layering of lava flows. Additionally, LP events have been identified in sub-horizontal cracks within an elongated structure that extends from SW to NE below the active vent (Zecevic et al.,

2016). Although this structure has a dip angle of around 45 degrees, it appears to be characterized by elevated sub-horizontal fracturing, which may influence the orientation of volcanic process-induced cracks. Further analyses are needed since the depth constraints of these crustal structures are not well resolved.

Chapter 7

SHORTCOMINGS AND FUTURE WORKS

Some of the challenges faced during this project include the depth constraints in our interpretation. We utilized 10 frequency bands and our observations of the earthquake and eruptive signals, which helped us to narrow down the depth ranges of our dv/v observations. Rayleigh and Love's waves are sensitive to different depths in the same frequency band. It is challenging to determine depths for scattered waves from sensitivity kernels because they are not fundamental modes of Rayleigh and Love waves. Additionally, our DRMS measurements have identified possible eruptive signals that we were unable to interpret due to poor data quality in the CCs. To improve our understanding of certain dv/v features detected during high DRMS and inconsistent dv/v behavior, additional broadband seismic stations could be incorporated into our dataset in the future if they are made available.

Chapter 8

SUMMARY

Ambient seismic noise interferometry (SNI) is a promising method to improve our understanding of complex crustal processes surrounding volcanic eruptions. SNI allows us to monitor the stress regime at volcanic settings by measuring long- and short-term changes in vertically (Vsh) and horizontally (Vsv) polarized shear waves. This technique enhances the reliability of existing surface tools to improve the forecasting of volcanic reawakening and limit its associated natural hazards in society. This research reveals varying crustal stress disturbance patterns in the Turrialba region linked to local earthquakes and eruptions. In this project, we utilized 14 broadband seismic stations to estimate changes in seismic wave velocity across a regional and local network. We used a local network to show our findings since it comprises stations atop Turrialba's summit which provides a more precise representation of crustal changes beneath the volcano. Our analysis involved 10 frequency bands for frequency-dependent analysis and the three seismic components to extract information from Rayleigh waves (ZZ) and Love waves (TT).

The earthquake event induced a higher velocity reduction in the local network in both seismic components and was more prominent at high-frequency bands. This observation suggests shallow crustal damage around the volcanic summit.

Observations in both seismic components, ZZ, and TT, indicate a radial pattern deformation since no notable differences in trend and magnitude are found. Besides, the long-lived velocity reduction in the area shows the impact of the seismic event on the stress stage of the crust beneath Turrialba. This long-lived crustal weakening could have played a key role in the alteration of this volcano's eruptive style since 2017. Moreover, while the connection between the Capellades earthquake and Turrialba is uncertain, the minor reduction in velocity during elevated DRMS and LP events that preceded the earthquake could indicate the involvement of volcanic processes in the seismic event's rupture process.

On the other hand, we identified in our dataset three potential eruptive signals (designated as (a), (b), and (c)) using DRMS estimations. However, we focused our analysis on signals a and b since signal c was influenced by a lack of seismic path density resulting from our quality control measures. During eruptive signals a and b, we discovered that the most significant dv/v changes were confined to the low-frequency ranges, indicating crustal deformation at greater depths compared to what was observed during the earthquake event. The nature of the velocity changes observed during the eruptive signals is attributed to the formation and closing of microcracks and pore fluids resulting from the pressurization and depressurization of the Turrialba's plumbing system. We proposed that the velocity reduction during signals a and b was caused by the creation of new cracks and pore fluids due to the high pressure of magmatic fluids at the base of the shallow magma system. In both scenarios, the introduction of fresh magmatic fluids increased the pressure at the

bottom of the shallow magma chamber, potentially rupturing any previous blockage in the conduit. We propose that during phase b, the pressure of the magmatic fluids was higher, indicated by the sudden drop in velocity and the burst in DRMS, ultimately resulting in an eruption in May 2016. Additionally, the observation of radial anisotropy patterns through the varying velocity trend in both ZZ and TT during eruptive signal b suggests a preferred orientation of crustal structures in the horizontal plane. This project is a crucial advancement in understanding the volcanic processes occurring beneath Turrialba, the impact of local earthquakes on stress distribution in the region, and how this can influence volcanic eruptive behavior, as well as identifying the orientation patterns of some subsurface structures at different depths.

REFERENCES

Alfaro, A., Denyer, P., Alvarado, G. E., Gazel, E., & Chamorro, C. (2018). Estratigrafía y petrografía de las rocas ígneas en el sector superior de la cordillera de Talamanca, Costa Rica. *Revista Geológica de América Central*, *58*. https://doi.org/10.15517/rgac.v58i0.32669

Alvarado, G. E., Brenes-André, J., Avard, G., Pereira, R., Galve, J. P., Campos-Durán, D., & de Moor, J. M. (2021). La actividad eruptiva del volcán Turrialba (Costa Rica) en el siglo XIX: reinterpretación de los documentos históricos y de los depósitos. *Revista Geológica de América Central*.

Ardhuin, F., Stutzmann, E., Schimmel, M., & Mangeney, A. (2011). Ocean wave sources of seismic noise. *Journal of Geophysical Research*, *116*(C9), C09004. https://doi.org/10.1029/2011JC006952

Aster, R. C., McNamara, D. E., & Bromirski, P. D. (2008). Multidecadal Climate-induced Variability in Microseisms. *Seismological Research Letters*, *79*(2), 194–202. https://doi.org/10.1785/gssrl.79.2.194

Aubouin, J., Von Huene, R., & et al. (1982). *Initial Reports of the Deep Sea Drilling Project, 67* (Vol. 67). U.S. Government Printing Office. https://doi.org/10.2973/dsdp.proc.67.1982

Avouris, D. M., Carn, S. A., & Waite, G. P. (2017). Triggering of volcanic degassing by large earthquakes. *Geology*, G39074.1. https://doi.org/10.1130/G39074.1

Battaglia, M., Alpala, J., Alpala, R., Angarita, M., Arcos, D., Euillades, L., Euillades, P., Muller, C., & Narváez, L. (2019). Monitoring Volcanic Deformation. In *Reference Module in Earth Systems and Environmental Sciences* (p. B9780124095489109029). Elsevier. https://doi.org/10.1016/B978-0-12-409548-9.10902-9

Bensen, G. D., Ritzwoller, M. H., Barmin, M. P., Levshin, A. L., Lin, F., Moschetti, M. P., Shapiro, N. M., & Yang, Y. (2007). Processing seismic ambient noise data to obtain reliable broad-band surface wave dispersion measurements. *Geophysical Journal International*, *169*(3), 1239–1260. https://doi.org/10.1111/j.1365-246X.2007.03374.x

Beyreuther, M., Barsch, R., Krischer, L., Megies, T., Behr, Y., & Wassermann, J. (2010). ObsPy: A Python Toolbox for Seismology. *Seismological Research Letters*, *81*(3), 530–533. https://doi.org/10.1785/gssrl.81.3.530

Brenguier, F., Rivet, D., Obermann, A., Nakata, N., Boué, P., Lecocq, T., Campillo, M., & Shapiro, N. (2016). 4-D noise-based seismology at volcanoes: Ongoing efforts and perspectives. *Journal of Volcanology and Geothermal Research*, *321*, 182–195. https://doi.org/10.1016/j.jvolgeores.2016.04.036

Brenguier, F., Shapiro, N. M., Campillo, M., Ferrazzini, V., Duputel, Z., Coutant, O., & Nercessian, A. (2008). Towards forecasting volcanic eruptions using seismic noise. *Nature Geoscience*, *1*(2), 126–130. https://doi.org/10.1038/ngeo104

Campillo, M., & Paul, A. (2003). Long-Range Correlations in the Diffuse Seismic Coda. *Science*, *299*(5606), 547–549. https://doi.org/10.1126/science.1078551

Carr, M. J., Feigenson, M. D., & Bennett, E. A. (1990). Incompatible element and isotopic evidence for tectonic control of source mixing and melt extraction along the Central American arc. *Contributions to Mineralogy and Petrology*, *105*(4), 369–380. https://doi.org/10.1007/BF00286825

Carr, M. J., Feigenson, M. D., Patino, L. C., & Walker, J. A. (2003). Volcanism and geochemistry in Central America: Progress and problems. In J. Eiler (Ed.), *Geophysical Monograph Series* (Vol. 138, pp. 153–174). American Geophysical Union. https://doi.org/10.1029/138GM09

Cayol, V., Dieterich, J. H., Okamura, A. T., & Miklius, A. (2000). High Magma Storage Rates Before the 1983 Eruption of Kilauea, Hawaii. *Science*, *288*(5475), 2343–2346. https://doi.org/10.1126/science.288.5475.2343

Chaves, E. J., & Schwartz, S. Y. (2016). Monitoring transient changes within overpressured regions of subduction zones using ambient seismic noise. *Science Advances*, *2*(1), e1501289. https://doi.org/10.1126/sciadv.1501289

Clarke, D., Zaccarelli, L., Shapiro, N. M., & Brenguier, F. (2011). Assessment of resolution and accuracy of the Moving Window Cross Spectral technique for monitoring crustal temporal variations using ambient seismic noise: MWCS: assessment of resolution and accuracy. *Geophysical Journal International*, *186*(2), 867–882. https://doi.org/10.1111/j.1365-246X.2011.05074.x

Colombi, A., Chaput, J., Brenguier, F., Hillers, G., Roux, P., & Campillo, M. (2014). On the temporal stability of the coda of ambient noise correlations. *Comptes Rendus Geoscience*, *346*(11–12), 307–316. https://doi.org/10.1016/j.crte.2014.10.002

Conde, V., Bredemeyer, S., Duarte, E., Pacheco, J. F., Miranda, S., Galle, B., & Hansteen, T. H. (2014). SO2 degassing from Turrialba Volcano linked to seismic signatures during the period 2008–2012. *International Journal of Earth Sciences*, *103*(7), 1983–1998. https://doi.org/10.1007/s00531-013-0958-5

de Moor, J. M., Aiuppa, A., Avard, G., Wehrmann, H., Dunbar, N., Muller, C., Tamburello, G., Giudice, G., Liuzzo, M., Moretti, R., Conde, V., & Galle, B. (2016). Turmoil at Turrialba Volcano (Costa Rica): Degassing and eruptive processes inferred from high-frequency gas monitoring: TURMOIL AT TURRIALBA VOLCANO. *Journal of Geophysical Research: Solid Earth*, *121*(8), 5761–5775. https://doi.org/10.1002/2016JB013150

DeMets, C. (2001). A new estimate for present-day Cocos-Caribbean Plate motion: Implications for slip along the Central American Volcanic Arc. *Geophysical Research Letters*, *28*(21), 4043–4046. https://doi.org/10.1029/2001GL013518

Donaldson, C., Caudron, C., Green, R. G., Thelen, W. A., & White, R. S. (2017). Relative seismic velocity variations correlate with deformation at Kīlauea volcano. *Science Advances*, *3*(6), e1700219. https://doi.org/10.1126/sciadv.1700219

Duputel, Z., Ferrazzini, V., Brenguier, F., Shapiro, N., Campillo, M., & Nercessian, A. (2009). Real time monitoring of relative velocity changes using ambient seismic noise at the Piton de la Fournaise volcano (La Réunion) from January 2006 to June 2007. *Journal of Volcanology and Geothermal Research*, *184*(1–2), 164–173. https://doi.org/10.1016/j.jvolgeores.2008.11.024

Duvall, T. L., Jeffferies, S. M., Harvey, J. W., & Pomerantz, M. A. (1993). Time–distance helioseismology. *Nature*, *362*(6419), 430–432. https://doi.org/10.1038/362430a0

Fichtner, A. (2014). Source and processing effects on noise correlations. *Geophysical Journal International*, *197*(3), 1527–1531. https://doi.org/10.1093/gji/ggu093

Fukao, Y., Nishida, K., Suda, N., Nawa, K., & Kobayashi, N. (2002). A theory of the Earth's background free oscillations: EARTH'S BACKGROUND FREE OSCILLATIONS. *Journal of Geophysical Research: Solid Earth*, *107*(B9), ESE 11-1-ESE 11-10. https://doi.org/10.1029/2001JB000153

Godfrey, H. J., Fry, B., & Savage, M. K. (2017). Shear-wave velocity structure of the Tongariro Volcanic Centre, New Zealand: Fast Rayleigh and slow Love waves indicate strong shallow anisotropy. *Journal of Volcanology and Geothermal Research*, *336*, 33–50. https://doi.org/10.1016/j.jvolgeores.2017.01.019

Goldstein, P., & Snoke, A. (2005). SAC availability for the IRIS community. *Incorporated Institutions for Seismology Data Management Center Electronic Newsletter*, *7*.

Gutenberg, B. (1936). On microseisms*. *Bulletin of the Seismological Society of America*, *26*(2), 111–117. https://doi.org/10.1785/BSSA0260020111

Herrmann, R. (2013). Computer Programs in Seismology: An Evolving Tool for Instruction and Research. *Seismological Research Letters*, *84*, 1081–1088. https://doi.org/10.1785/0220110096

Lecocq, T., Caudron, C., & Brenguier, F. (2014). MSNoise, a Python Package for Monitoring Seismic Velocity Changes Using Ambient Seismic Noise. *Seismological Research Letters*, *85*(3), 715–726. https://doi.org/10.1785/0220130073

Lecocq, T., Hicks, S. P., Van Noten, K., Van Wijk, K., Koelemeijer, P., De Plaen, R. S. M., Massin, F., Hillers, G., Anthony, R. E., Apoloner, M.-T., Arroyo-Solórzano, M., Assink, J. D., Büyükakpınar, P., Cannata, A., Cannavo, F., Carrasco, S., Caudron, C., Chaves, E. J., Cornwell, D. G., … Xiao, H. (2020). Global quieting of high-frequency seismic noise due to COVID-19 pandemic lockdown measures. *Science*, *369*(6509), 1338–1343. https://doi.org/10.1126/science.abd2438

Lénat, J.-F., Bachèlery, P., & Peltier, A. (2012). The interplay between collapse structures, hydrothermal systems, and magma intrusions: The case of the central area of Piton de la Fournaise volcano. *Bulletin of Volcanology*, *74*(2), 407–421. https://doi.org/10.1007/s00445-011-0535-3

Lesage, P., Reyes-Dávila, G., & Arámbula-Mendoza, R. (2014). Large tectonic earthquakes induce sharp temporary decreases in seismic velocity in Volcán de Colima, Mexico: VELOCITY VARIATIONS IN VOLCANO. *Journal of Geophysical Research: Solid Earth*, *119*(5), 4360–4376. https://doi.org/10.1002/2013JB010884

Lin, F.-C., Moschetti, M. P., & Ritzwoller, M. H. (2008). Surface wave tomography of the western United States from ambient seismic noise: Rayleigh and Love wave phase velocity maps. *Geophysical Journal International*, *173*(1), 281–298. https://doi.org/10.1111/j.1365-246X.2008.03720.x

Liu, G., Fomel, S., Jin, L., & Chen, X. (2009). Stacking seismic data using local correlation. *GEOPHYSICS*, *74*(3), V43–V48. https://doi.org/10.1190/1.3085643

Liu, Z., Huang, J., Peng, Z., & Su, J. (2014). Seismic velocity changes in the epicentral region of the 2008 Wenchuan earthquake measured from three-component ambient noise correlation techniques: TEMPORAL CHANGES IN WENCHUAN EPICENTER. *Geophysical Research Letters*, *41*(1), 37–42. https://doi.org/10.1002/2013GL058682

Martini, F., Tassi, F., Vaselli, O., Del Potro, R., Martinez, M., del Laat, R. V., & Fernandez, E. (2010). Geophysical, geochemical and geodetical signals of reawakening at Turrialba volcano (Costa Rica) after almost 150years of quiescence. *Journal of Volcanology and Geothermal Research*, *198*(3–4), 416–432. https://doi.org/10.1016/j.jvolgeores.2010.09.021

Mick, E., Stix, J., De Moor, J. M., & Avard, G. (2021). *Hydrothermal alteration and sealing at Turrialba as a mechanism for phreatic eruption triggering* [Other]. pico. https://doi.org/10.5194/egusphere-egu21-107

Mordret, A., Jolly, A. D., Duputel, Z., & Fournier, N. (2010). Monitoring of phreatic eruptions using Interferometry on Retrieved Cross-Correlation Function from Ambient Seismic Noise: Results from Mt. Ruapehu, New Zealand. *Journal of Volcanology and Geothermal Research*, *191*(1–2), 46–59. https://doi.org/10.1016/j.jvolgeores.2010.01.010

Mordret, A., Rivet, D., Landès, M., & Shapiro, N. M. (2015). Three-dimensional shear velocity anisotropic model of Piton de la Fournaise Volcano (La Réunion Island) from ambient seismic noise. *Journal of Geophysical Research: Solid Earth*, *120*(1), 406–427. https://doi.org/10.1002/2014JB011654

Olivier, G., & Brenguier, F. (2016). Interpreting seismic velocity changes observed with ambient seismic noise correlations. *Interpretation*, *4*(3), SJ77–SJ85. https://doi.org/10.1190/INT-2015-0203.1

O'Neel, S., Marshall, H. P., McNamara, D. E., & Pfeffer, W. T. (2007). Seismic detection and analysis of icequakes at Columbia Glacier, Alaska. *Journal of Geophysical Research: Earth Surface*, *112*(F3). https://doi.org/10.1029/2006JF000595

Poupinet, G., Ellsworth, W. L., & Frechet, J. (1984). Monitoring velocity variations in the crust using earthquake doublets: An application to the Calaveras Fault, California. *Journal of Geophysical Research: Solid Earth*, *89*(B7), 5719–5731. https://doi.org/10.1029/JB089iB07p05719

Protti, M., McNally, K., Pacheco, J., González, V., Montero, C., Segura, J., Brenes, J., Barboza, V., Malavassi, E., Güendel, F., Simila, G., Rojas, D., Velasco, A., Mata, A., & Schillinger, W. (1995). The March 25, 1990 (M_w = 7.0, M_L =

6.8), earthquake at the entrance of the Nicoya Gulf, Costa Rica: Its prior activity, foreshocks, aftershocks, and triggered seismicity. *Journal of Geophysical Research: Solid Earth*, *100*(B10), 20345–20358. https://doi.org/10.1029/94JB03099

Ratdomopurbo, A., & Poupinet, G. (1995). Monitoring a temporal change of seismic velocity in a volcano: Application to the 1992 eruption of Mt. Merapi (Indonesia). *Geophysical Research Letters*, *22*(7), 775–778. https://doi.org/10.1029/95GL00302

Reagan, M., Duarte, E., Soto, G. J., & Fernández, E. (2006). The eruptive history of Turrialba volcano, Costa Rica, and potential hazards from future eruptions. In W. I. Rose, G. J. S. Bluth, M. J. Carr, J. W. Ewert, L. C. Patino, & J. W. Vallance, *Volcanic Hazards in Central America*. Geological Society of America. https://doi.org/10.1130/2006.2412(13)

Rhie, J., & Romanowicz, B. (2004). Excitation of Earth's continuous free oscillations by atmosphere–ocean–seafloor coupling. *Nature*, *431*(7008), 552–556. https://doi.org/10.1038/nature02942

Rivet, D., Brenguier, F., Clarke, D., Shapiro, N. M., & Peltier, A. (2014). Long-term dynamics of Piton de la Fournaise volcano from 13 years of seismic velocity change measurements and GPS observations. *Journal of Geophysical Research: Solid Earth*, *119*(10), 7654–7666. https://doi.org/10.1002/2014JB011307

Roman, D. C., & Cashman, K. V. (2018). Top–Down Precursory Volcanic Seismicity: Implications for 'Stealth' Magma Ascent and Long-Term Eruption Forecasting. *Frontiers in Earth Science*, *6*, 124. https://doi.org/10.3389/feart.2018.00124

Rouwet, D., Mora-Amador, R., Ramírez, C., González, G., Baldoni, E., Pecoraino, G., Inguaggiato, S., Capaccioni, B., Lucchi, F., & Tranne, C. A. (2021). Response of a hydrothermal system to escalating phreatic unrest: The case of Turrialba and Irazú in Costa Rica (2007–2012). *Earth, Planets and Space*, *73*(1), 142. https://doi.org/10.1186/s40623-021-01471-8

Rubinstein, J. L., & Beroza, G. C. (2005). Depth constraints on nonlinear strong ground motion from the 2004 Parkfield earthquake: DEPTH CONSTRAINTS ON NONLINEARITY. *Geophysical Research Letters*, *32*(14), n/a-n/a. https://doi.org/10.1029/2005GL023189

Saginor, I., Gazel, E., Condie, C., & Carr, M. J. (2013). Evolution of geochemical variations along the Central American volcanic front: CENTRAL

AMERICAN GEOCHEMICAL VARIATIONS. *Geochemistry, Geophysics, Geosystems*, *14*(10), 4504–4522. https://doi.org/10.1002/ggge.20259

Seropian, G., Kennedy, B. M., Walter, T. R., Ichihara, M., & Jolly, A. D. (2021). A review framework of how earthquakes trigger volcanic eruptions. *Nature Communications*, *12*(1), 1004. https://doi.org/10.1038/s41467-021-21166-8

Shapiro, N. M., & Campillo, M. (2004). Emergence of broadband Rayleigh waves from correlations of the ambient seismic noise. *Geophysical Research Letters*, *31*(7). https://doi.org/10.1029/2004GL019491

Shapiro, N. M., Campillo, M., Stehly, L., & Ritzwoller, M. H. (2005). High-Resolution Surface-Wave Tomography from Ambient Seismic Noise. *Science*, *307*(5715), 1615–1618. https://doi.org/10.1126/science.1108339

Snieder, R. (2004). Extracting the Green's function from the correlation of coda waves: A derivation based on stationary phase. *Physical Review E*, *69*(4), 046610. https://doi.org/10.1103/PhysRevE.69.046610

Stehly, L., Fry, B., Campillo, M., Shapiro, N. M., Guilbert, J., Boschi, L., & Giardini, D. (2009). Tomography of the Alpine region from observations of seismic ambient noise. *Geophysical Journal International*, *178*(1), 338–350. https://doi.org/10.1111/j.1365-246X.2009.04132.x

Stix, J., & De Moor, J. M. (2018). Understanding and forecasting phreatic eruptions driven by magmatic degassing. *Earth, Planets and Space*, *70*(1), 83. https://doi.org/10.1186/s40623-018-0855-z

Taisne, B., Brenguier, F., Shapiro, N. M., & Ferrazzini, V. (2011). Imaging the dynamics of magma propagation using radiated seismic intensity: DYNAMICS OF DIKE PROPAGATION. *Geophysical Research Letters*, *38*(4), n/a-n/a. https://doi.org/10.1029/2010GL046068

Tobias Megies, Moritz Beyreuther, Robert Barsch, Lion Krischer, & Joachim Wassermann. (2011). ObsPy – What can it do for data centers and observatories? *Annals of Geophysics*, *54*(1). https://doi.org/10.4401/ag-4838

Tsai, V. C. (2009). On establishing the accuracy of noise tomography travel-time measurements in a realistic medium. *Geophysical Journal International*, *178*(3), 1555–1564. https://doi.org/10.1111/j.1365-246X.2009.04239.x

Universidad de Costa Rica, San Pedro, Costa Rica, Linkimer, L., Arroyo, I. G., Universidad de Costa Rica, San Pedro, Costa Rica, Soto, G. J., Universidad de Costa Rica, San Pedro, Costa Rica, Porras, J. L., Universidad de Costa Rica,

San Pedro, Costa Rica, Araya, M. C., Universidad de Costa Rica, San Pedro, Costa Rica, Mora, M. M., Universidad de Costa Rica, San Pedro, Costa Rica, Taylor, M., & Universidad de Costa Rica, San Pedro, Costa Rica. (2018). El sismo de Capellades del 2016 y su secuencia sísmica: Manifestación de fallamiento de rumbo en el arco volcánico de Costa Rica. *Boletín de Geología*, *40*(2), 35–53. https://doi.org/10.18273/revbol.v40n2-2018002

Van Der Laat, L., Mora, M. M., Pacheco, J. Fco., Lesage, P., & Meneses, E. (2022). Seismicity during the recent activity (2009–2020) of Turrialba volcano, Costa Rica. *Journal of Volcanology and Geothermal Research*, *431*, 107651. https://doi.org/10.1016/j.jvolgeores.2022.107651

Wang, Q., Campillo, M., Brenguier, F., Lecointre, A., Takeda, T., & Hashima, A. (2019). Evidence of Changes of Seismic Properties in the Entire Crust Beneath Japan After the M_w 9.0, 2011 Tohoku-oki Earthquake. *Journal of Geophysical Research: Solid Earth*, *124*(8), 8924–8941. https://doi.org/10.1029/2019JB017803

Wang, Q.-Y., Brenguier, F., Campillo, M., Lecointre, A., Takeda, T., & Aoki, Y. (2017). Seasonal Crustal Seismic Velocity Changes Throughout Japan: SEASONAL SEISMIC VELOCITY CHANGES. *Journal of Geophysical Research: Solid Earth*, *122*(10), 7987–8002. https://doi.org/10.1002/2017JB014307

Weaver, R. L., Hadziioannou, C., Larose, E., & Campillo, M. (2011). On the precision of noise correlation interferometry: Precision of noise correlation interferometry. *Geophysical Journal International*, *185*(3), 1384–1392. https://doi.org/10.1111/j.1365-246X.2011.05015.x

Wegler, U., Nakahara, H., Sens-Schönfelder, C., Korn, M., & Shiomi, K. (2009). Sudden drop of seismic velocity after the 2004 Mw 6.6 mid-Niigata earthquake, Japan, observed with Passive Image Interferometry. *Journal of Geophysical Research: Solid Earth*, *114*(B6). https://doi.org/10.1029/2008JB005869

Welch, P. (1967). The use of fast Fourier transform for the estimation of power spectra: A method based on time averaging over short, modified periodograms. *IEEE Transactions on Audio and Electroacoustics*, *15*(2), 70–73. https://doi.org/10.1109/TAU.1967.1161901

Wu, C., Delorey, A., Brenguier, F., Hadziioannou, C., Daub, E. G., & Johnson, P. (2016). Constraining depth range of *S* wave velocity decrease after large earthquakes near Parkfield, California: DEPTH RANGE OF *S* WAVE

VELOCITY DECREASE. *Geophysical Research Letters*, *43*(12), 6129–6136. https://doi.org/10.1002/2016GL069145

Wu, C., & Peng, Z. (2011). Temporal changes of site response during the 2011 M w 9.0 off the Pacific coast of Tohoku Earthquake. *Earth, Planets and Space*, *63*(7), 791–795. https://doi.org/10.5047/eps.2011.06.011

Yang, Y., Ritzwoller, M. H., Levshin, A. L., & Shapiro, N. M. (2007). Ambient noise Rayleigh wave tomography across Europe. *Geophysical Journal International*, *168*(1), 259–274. https://doi.org/10.1111/j.1365-246X.2006.03203.x

Zecevic, M., De Barros, L., Eyre, T. S., Lokmer, I., & Bean, C. J. (2016). Relocation of long-period (LP) seismic events reveals en echelon fractures in the upper edifice of Turrialba volcano, Costa Rica. *Geophysical Research Letters*, *43*(19). https://doi.org/10.1002/2016GL070427

Appendix A

PARAMETERS FOR SIGNAL PROCESSING

A.1 Station-pair dataset Preprocessing Parameters (MSNoise version 1.6.1)

Parameter	Description	Value
analysis duration	Duration of analysis	86,400 seconds
autocorr	Compute auto-correlations	No
cc_sampling_rate	Sampling rate for CCFs	20
channels	Seismic channels	HHE, HHN, HHZ
componets_to_compute	Seismic components used in the cross-correlation	ZZ, RR, TT
corr_duration	Length of data windows to correlate	1,800 seconds
dtt_lag	How the lag time is defined (dynamic or static)	Static
dtt_maxdt	Maximum delay time measurement	0.1
dtt_maxerr	Minimum error on delay time measurement	0.1
dtt_mincoh	Minimum coherence on delay time measurement	0.7
dtt_minlag	Minimum lag for delay time measurements	5
dtt_sides	Which sides of CCFs to use for delay times	Both
dtt_width	Width of time lag window	30 seconds
enddate	End date of data	2018-01-01
maxlag	Maximum lag of CCFs	120 seconds
mov_stack	Stack size	2,5,10 days
preprocess_highpass	Preprocessing high-pass value	0.01Hz
preprocess_lowpass	Preprocessing low-pass value	8 Hz
ref_begin	Reference stack start date	2015-02-01

ref_end	Reference stack end date	2016-10-01
resampling_method	Resampling method (decimate / lanczos)	Lanczos
stack_method	Stack Method: Linear mean or phase weighted stack	Linear
startdate	Start date of data	2015-01-01
whitening	Whiten Traces before cross-correlation	All
windsorizing	Windorizing at N times RMS	3

A.2 Examples of Turrialba dataset parameters used during the Moving-Window Cross Spectral analysis step in the 0.6–0.8 Hz frequency band.

Parameter	**Description**	**Value**
Low	The lower frequency bound of the whiten function	0.01Hz
Mwcs low	The lower frequency bound of the linear regression done in MWCS	0.6 Hz
Mwcs high	The upper frequency bound of the linear regression done in MWCS	0.8 Hz
High	The upper frequency bound of the whiten function	8.0 Hz
Mwcs wlen	Window length to perform MWCS	20.0 seconds
Mwcs step	Step of the windowing procedure in MWCS	5.0 seconds